A Lagrangian description of transport associated with a Front-Eddy interaction: application to data from the North-Western Mediterranean Sea

Michał Branicki
School of Mathematics, University of Bristol,
Bristol BS8 1TW, United Kingdom
Ana M. Mancho
Instituto de Ciencias Matemáticas (CSIC-UAM-UC3M-UCM)
Serrano 121, 28006 Madrid, Spain
Stephen Wiggins
School of Mathematics, University of Bristol,
Bristol BS8 1TW, United Kingdom

May 12, 2008

Abstract

We continue the study started in [28] of Lagrangian transport in the Northwestern Mediterranean Sea, near the North Balearic Front, using the velocity field obtained from a numerical simulation of the surface circulation. The analysis is carried out within the framework of dynamical systems theory. We focus on transport associated with the interaction of the front with one or two eddies. The numerical simulation provides us with an Eulerian view of the flow and we use the dynamical systems approach to identify relevant hyperbolic trajectories and their stable and unstable manifolds which are used to give a Lagrangian construction of the front-eddy system. Transport in the system is effected by the turnstile mechanism whose evolution reveals the spatio-temporal routes along which transport occurs. We show that different transport routes are possible depending on whether the current interacts with one or two eddies. We also consider the transport implications associated with the transition between the one and two eddy situation. We introduce a kinematic model that provides insight into the nature of the change in hyperbolic trajectories and their stable and unstable manifolds associated with the "birth and death" of eddies. Finally, guided by our particular data set, we introduce a more complicated kinematic model that provides us with the ability to "control" the Eulerian flow features in a way that enables us to more deeply explore their implications for Lagrangian transport in other complicated front-eddy systems which are abundant in oceanic flows.

1 Introduction

Advances in observational methods and computational resources have revealed a variety of flow structures in the ocean, such as jets, fronts, and eddies, that exhibit nontrivial evolution in space and time. Recent observations and experiments indicate

that these structures significantly influence transport characteristics of the flow, see, for example [42]. The global, geometrical framework of nonlinear dynamical systems theory has proven to be useful for analyzing transport issues in such flows as it is concerned with issues associated with the role that localized structures play in influencing the motions of collections of trajectories in space and time. However, the application of this mathematical approach to "realistic" geophysical flows has required the development of new concepts in dynamical systems theory-so called "finite-time dynamical systems". Recent reviews of this framework in the context of oceanographic flows can be found in [44, 30, 40], and we briefly discuss the relevant issues at the beginning of §3.

The geophysical flow structure that has been the subject of extensive analysis from the dynamical systems point of view is the zonally propagating jet. Beginning with the work of Bower [4], a variety of kinematic models of jets have been considered ([41, 13, 14, 32, 5]). This work paved the way for the development of tools and concepts for the analysis of transport in dynamically consistent models of jets ([37, 45, 46]). The insight and mathematical ideas developed in that body of work were then used to develop a deeper understanding of the Gulf Stream from observational data by Lozier et al. [25]. This progression of work on transport in zonally propagating jets illustrates the power and flexibility of the dynamical systems approach. Whether the flow is realized as a kinematic model, dynamical model, or a model obtained from observations, the approach of dynamical systems theory is the same in each case since the specific form of the velocity field under consideration is not the main issue. Rather, the analysis proceeds after the identification of certain specific geometrical structures in the flow and their characterization in terms of dynamical systems ideas and tools.

The zonally propagating jet work has been a fertile test bed for the development of the notion of a "finite-time dynamical system". In this context, the key concepts for describing and quantifying the Lagrangian transport properties of the jet were finite-time hyperbolic trajectories (roughly, "moving saddle points") and their finite-time stable and unstable manifolds (roughly, material surfaces that control the movement of fluid associated with jet). In [28] this approach was used to study transport associated with a front in the North-Western Mediteranean Sea using a high resolution numerical ocean model developed in [11, 12, 15]. It was shown there that the dynamical systems approach could be used to give a geometrical characterization of the front in a manner that allowed both qualitative and quantitative analyses of transport properties. In particular, it was shown that the location of the front could be identified as a "Lagrangian barrier" across which transport is small. Moreover, transport to, across, and away from the front occurred by a complex spatio-temporal route of filaments that could be described and quantified with the ideas of lobe dynamics. In [28] the Lagrangian front was the only analysed structure. The authors pointed out, however, that transport across the front could be affected by nearby eddies.

The purpose of this paper is to continue the work on transport in the North-Western Mediterranean Sea (c.f. [28]) by considering the transport properties in the situation where the front interacts with one, or two, eddies. In particular, data provided by the numerical ocean model shows that there is a period of time when the front interacts significantly with a single eddy (which we refer to as "Scenario I"), and a period of time when the front significantly interacts with a pair of eddies (referred to as "Scenario II").

There is an important concept that we must address and develop further in this paper. While the Lagrangian description of jets and fronts in the context of dynamical systems theory is well established, a Lagrangian description of an eddy, in a way that

enables us to describe and quantify the motion of fluid "towards" and "away from" an eddy, as well as its emergence and disappearance, has not been carefully developed. We will provide such a definition in this paper that is appropriate for our needs. We remark that the "Lagrangian description of an eddy" is a topic of current importance as a result of recently obtained data sets showing that eddies play a very important role in transport processes in the ocean ([7]). While a Lagrangian description of eddies is important for understanding issues associated with transport, it proves to be difficult to relate this to the typical intuitive understanding of eddies which usually derives from an Eulerian description. This issue becomes particularly problematic when, from Eulerian observations, one sees the appearance and disappearance of eddies. In some cases these events are a signature of a Lagrangian transition in the flow (e.g. in the transition between Scenarios I and II discussed later). However, there is no general relationship between the Eulerian and Lagrangian transitions and it is impossible to determine purely from the Eulerian observations whether a birth of an Eulerian eddy was accompanied by a change in the underlying Lagrangian flow structure, controlling transport. In this context we will present a kinematic model that will serve to isolate and highlight some of the main issues and provide guidance when we consider more complex velocity fields.

The structure of the paper is as follows. In §2 we describe the relevant Eulerian flow features which lead to identification of the front-eddy system in the velocity field that is the output of a high resolution model of the Mediterranean Sea. In §3 we introduce the dynamical systems tools required to describe transport in the front-eddy system. This enables us to describe precisely what we mean by Scenario I and Scenario II, from a Lagrangian point of view, as well as the issues associated with the transition between these scenarios. It is also in this section where we discuss the Lagrangian description of an eddy. In §4 we use the tools of §3 to describe transport in the realistic, numerical model of the Mediterranean introduced in §2. In §5 we develop and discuss a kinematic model of the front-eddy interaction that encompasses Scenarios I and II, as well as the transition between these scenarios. The kinematic model provides an ideal "laboratory" for studying eddy-front interactions as it enables us to easily study a variety of flow situations in a "controlled" manner in a way that cannot be done for of the output of the high resolution numerical model. The results of such studies will provide insight into how to understand and analyse transport in these more complex models. Finally §6 presents the conclusions as well as describes outstanding issues and directions for future work.

2 The Ocean Circulation Model and the Eulerian Structures of Interest

The details of the numerical model, sufficient for our purposes, can be found in [28], but we provide a brief summary of features that may be of immediate interest for this work.

The velocity field that we study is obtained from an ocean model, DieCAST [11], adapted to the Mediterranean Sea [12, 15]. The model uses the 3D primitive equations and is discretized with a fourth-order collocated control volume method. Details of boundary conditions, physical parameters such as horizontal and vertical viscosity and diffusivity, and the various types of forcing can be found in the above references.

The horizontal resolution is the same in both the longitudinal (ϕ) and latitudinal (λ) directions, with $\Delta\phi$= (1/8) of degree and $\Delta\lambda = \Delta\phi\cos\lambda$ thus making square

horizontal control volume boundaries. The vertical resolution is variable, with 30 control volume layers. The thickness of control volumes in the top layer is 10.3 m and they are smoothly increased up to the deepest bottom control volume face at 2750 m.

The model is initialized at a state of rest and the spin-up phase of integration is carried out for 16 years. Each year is considered to have 12 months of 30 days length each (i.e. 360 days).

We focus on velocity fields obtained at the second layer which has its center at a depth of 15.93 m. This is representative of the surface circulation and is not as directly driven by wind as the top layer.

The velocity field has small vertical components, so therefore this is not strictly a two dimensional flow. Vertical velocities of the order of 10^{-5} m/s, and it is argued in [28] that, as a rule of thumb, we can consider that trajectories preserve two dimensionality during time intervals of about 20 days. Therefore we will restrict our trajectory integrations to time intervals below that duration, and therefore they can be considered two dimensional to a good approximation. Details of how trajectories were calculated can be found in [28].

Figure 1 shows the velocity field at day 679 (the 19th day of the eleventh month – November – of the second year). The instantaneous stagnation points (ISPs) are displayed: the hyperbolic ISPs (i.e. saddle points in the linear, frozen-time approximation) are denoted with a cross and the elliptic ISPs (i.e. stable points in the linear (frozen-time) approximation) are denoted with a gray dot. The area of interest is located in the Western Mediterranean Sea and the Eulerian current studied in [28] is highlighted with the dark straight line. At the Eastern end of the dark straight line we show a dark circle surrounding an elliptic ISP, which we recognize as the Eulerian signature of an eddy.

Figure 2 shows the velocity field at day 683 (the 23rd day of the eleventh month – November – of the second year). We illustrate the same Eulerian features as in 1, but we also highlight a smaller (Eulerian) eddy (marked with a small dark circle) that has appeared after a saddle node bifurcation of ISPs at day 680 (the signature that the saddle-node bifurcation of ISPs occurred is the additional pair of ISPs, one saddle and one elliptic, at the Eastern end of the straight line).

Our goal is to understand the Lagrangian transport features associated with scenarios I and II, as well as how they change in the transition between these two scenarios. In order to do this, we will need to develop a Lagrangian characterization of these Eulerian features, and we will develop the tools and concepts for doing this in the next section. However, it is important to realize that our Lagrangian analysis is guided by the Eulerian features of the data set.

3 Dynamical Systems perspective of Lagrangian transport

In this section we recall the basic tools from dynamical systems theory that we will use to analyse Lagrangian transport of the front-eddy system. Following many earlier works using the dynamical systems approach for analyzing Lagrangian transport in unsteady flows (see references in §1), the notion of hyperbolicity is central to our analysis and it provides the means for characterizing trajectories in time-dependent flows which behave like "moving saddle points". These hyperbolic trajectories have

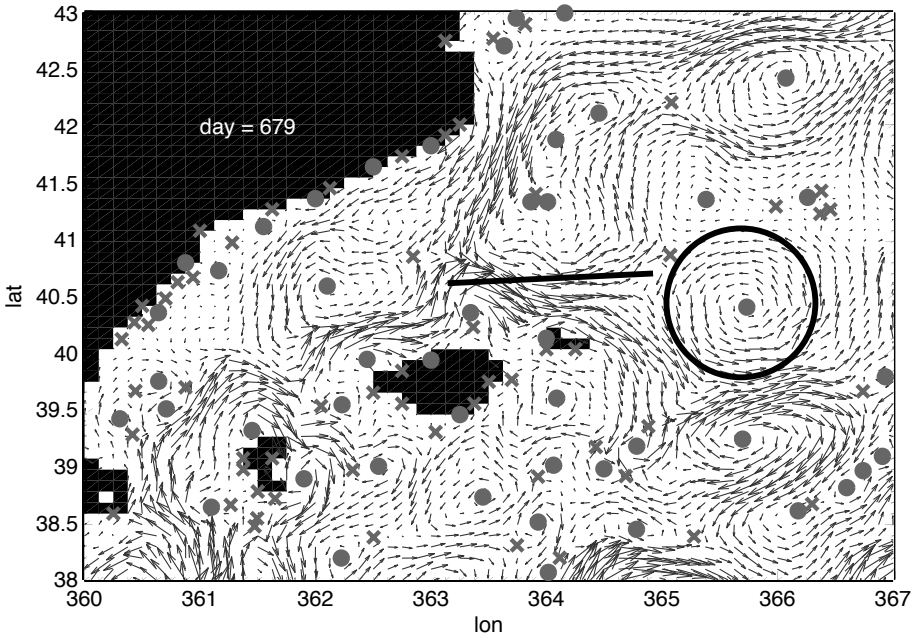

Figure 1: **DieCAST model, NW Mediterranean.** The velocity field at day 679 showing the Eulerian current (denoted by the dark line) studied in [28] as well as an Eulerian eddy at the eastern end of the current. This situation is often associated with a Lagrangian flow structure referred to hereafter as Scenario I. In this figure the dark regions represent land. The large dark region of the upper left hand corner is Spain, the large island in the middle is Majorca, the small island to the right of Majorca is Menorca, and the island to the left of Majorca is Ibiza.

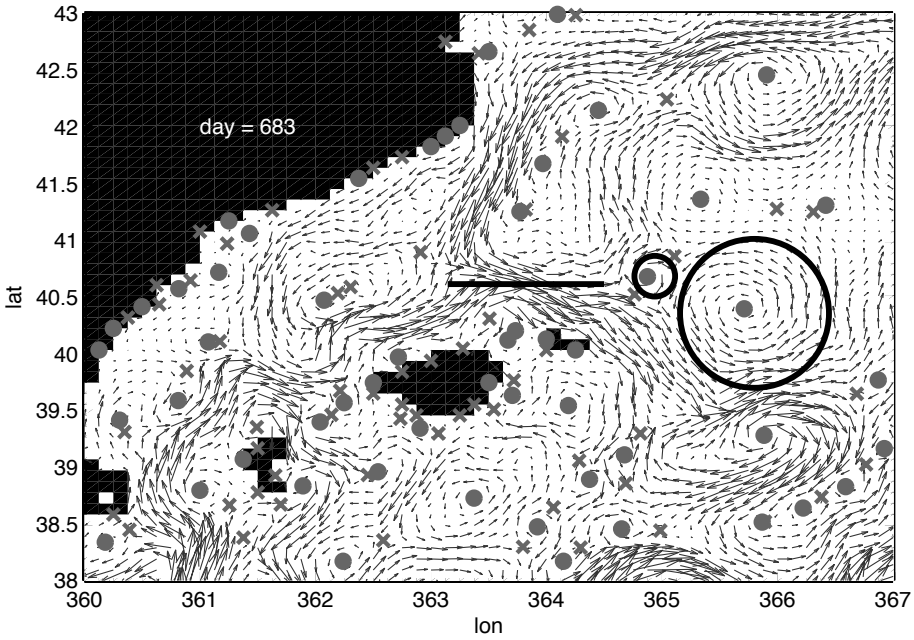

Figure 2: The velocity field at day 683 highlighting the same Eulerian features as for day 679, but with an additional (small) Eulerian eddy at the eastern end of the current resulting from the creation a new elliptic ISP in a saddle-node bifurcation at day 680. This situation is often associated with existence a Lagrangian structure referred to later as Scenario II.

stable and unstable invariant manifolds[1] which, similarly to the separatrix manifolds of saddle points in steady flows, can be used to identify boundaries between distinct regions in the flow domain. In particular, we will use the stable and unstable manifolds of particularly relevant hyperbolic trajectories, the so-called Distinguished Hyperbolic Trajectories (DHTs), to construct a Lagrangian front, i.e. an elongated transport barrier which strongly inhibits transport across it (here we follow [28]), and a Lagrangian eddy characterised by an area of predominantly recirculating flow. From this construction we will be able to understand transport characteristics of different configurations involving a front and an eddy (or eddies) by following the time evolution of the so-called *turnstile lobes*. The geometry of turnstile lobes associated with different Lagrangian structures will also give us the means for determining whether an 'interaction' between coexisting coherent structures actually takes place and we will show that they are the mechanism for understanding the spatio-temporal routes of transport associated with the front-eddy system.

However, a word of caution is in order here. Dynamical systems theory is often described as the study of the "long time" or "asymptotic" behaviour of systems. Indeed, the notions of "hyperbolicity" and "stable and unstable manifolds of hyperbolic trajectories" are concepts that are defined in the limit as time goes to plus or minus infinity. Hence, these notions would appear to be somewhat problematic when considering applications to time-dependent velocity fields that are only defined for a finite time. The original applications of dynamical systems theory to the study of transport in flows was for two dimensional time-periodic or three dimensional steady flows (for some history see [1, 44, 30]). In these settings the flow was clearly known for "all time". However, as mentioned at the beginning of the introduction, the case for applying this approach to the study of Lagrangian transport in geophysical flows defined as data sets obtained from either numerical computation or experimental measurement is compelling, and it has necessitated the development of the notion of a "finite-time dynamical system". In this setting notions of finite-time hyperbolic trajectories and finite-time stable and unstable manifolds have been proposed (see, e.g., [33, 20, 16, 9, 22, 29]), and they have proven to give useful insight and quantitative predictions in geophysical flows defined as finite time data sets (cf. the "story of the jet" discussed in the introduction, and considered in some detail in [44, 30, 40]). Nevertheless, these finite-time concepts are somewhat different from their infinite time counterparts. The main difference is a loss of uniqueness of relevant hyperbolic structures that arises from the inability to consider asymptotic limits[2]. This means that for any hyperbolic trajectory on a finite time interval there exists a neighbourhood of finite-time stable and unstable manifolds associated with this trajectory, with the size of these neighbourhoods shrinking to zero in the asymptotic limit (thus giving unique stable and unstable manifolds). These issues are discussed in [33, 20, 16, 9, 22, 29]. For our analysis this is not really a severe limitation since our finite-time hyperbolic trajectories are fluid particle trajectories. Consequently, the particular finite-time stable and unstable manifolds that we compute for these trajectories are "material surfaces" in the extended phase space (x, y, t) and we show directly their relevance to transport in the front-eddy system[3].

[1] In fluid mechanical terminology the phrase "invariant manifold" is synonomous with "material surface" (in our setting the surface is a curve) and "stable and unstable" refer to the behaviour of trajectories on the appropriate material surface, which we will describe shortly.

[2] Of course, one could argue that practically one realizes these notions through a numerical computation, which is necessarily a finite-time realization. However, making this assertion mathematically precise requires some considerable work that is beyond the scope of this paper, and much of which has not yet been undertaken (but see [18]).

[3] To avoid confusion with the classical, infinite time, notions of hyperbolicity and stable and unsta-

For completeness, we will recall the basic notions from dynamical systems theory that will form the fundamental building blocks for our analysis of Lagrangian transport.

3.1 The Basic "building blocks" from dynamical systems theory for analyzing Lagrangian transport

Recall that the Eulerian flow features we identify in the data obtained from the DieCAST ocean model can be regarded as two-dimensional to a good approximation during the time interval considered (about 20 days; see §2). We thus recall the most important notions used to develop the Lagrangian characterisation of these features in their two-dimensional formulation. However, most of these tools can be generalised and applied to three-dimensional flows.

First we describe the "Eulerian notion" of an instantaneous stagnation point. While these are (generally) not fluid particle trajectories, they may be useful "signatures" associated with Eulerian structures which suggest a need for a Lagrangian transport analysis.

Hyperbolic instantaneous stagnation points (ISP's).

Consider a dynamical system, associated with a two-dimensional velocity field $\mathbf{v}$, given by

$$\dot{\mathbf{x}} = \mathbf{v}(\mathbf{x}, t), \quad \mathbf{x} \in \mathscr{D}, \quad t \in [t_i,\ t_f] \equiv \mathcal{T}, \tag{1}$$

where $\mathscr{D} \subset I\!R^2$ is the domain of $\mathbf{v}$, and $\mathcal{T}$ denotes the time interval over which the flow is defined. Note here that we explicitly assume that the system (1) is defined over a finite-time interval (i.e. $t_i, > -\infty$, $t_f < \infty$) which has important consequences in further considerations.

An *instantaneous stagnation point* corresponds to a point in space, $\mathbf{x}^* \in \mathscr{D}$, such that at a fixed time $t^* \in \mathcal{T}$ we have

$$\mathbf{v}(\mathbf{x}^*, t^*) = 0. \tag{2}$$

We say that an ISP is (frozen-time) hyperbolic if the Jacobian matrix of the linearization about $\mathbf{x}^*$ at a fixed time t^*, i.e. $\partial \mathbf{v}(\mathbf{x}, t^*)/\partial \mathbf{x}|_{\mathbf{x}=\mathbf{x}^*}$, has two real, non-zero eigenvelues. (For 2D, incompresible flows this reduces to a requirement that the eigenvalues are of equal magnitudes but opposite signs). If the eigenvalues are pure imaginary and complex conjugates of each other, we say that the corresponding ISP is (frozen-time) elliptic. It turns out that, for as long as the ISP remains hyperbolic, one can continue a unique curve of ISPs in time (i.e. a path of ISPs in the extended phase space (x, y, t)), which is given implicitly by

$$\mathbf{v}(\mathbf{x}_{\rm isp}(t), t) = 0, \qquad t \in \tilde{\mathcal{T}}, \tag{3}$$

where $\tilde{\mathcal{T}} \subset \mathcal{T}$ is a time interval within which the Jacobian, $\left|\partial \mathbf{v}(\mathbf{x}, t)/\partial \mathbf{x}|_{\mathbf{x}=\mathbf{x}_{\rm isp}(t)}\right|$, does not vanish, as required by the Implicit Function Theorem (see [30] for more information and further references). It is often the case that the Jacobian of the (frozen-time)

ble manifolds from dynamical systems theory one might think it would be less confusing to adopt new names for the analogous notions in the finite-time setting. Perhaps this would be a better approach, but at this point the terminology is fairly pervasive throughout the literature and new terminology could be even more confusing. In [40] an attempt is made to deal with this through the use of the phrase "material manifold", and this precisely describes a key feature of the relevance of these curves to fluid transport.

linearisation about a hyperbolic ISP vanishes at some time, say $t = \tilde{t}$, as the path of ISPs is continued either forward or backward in time. Such points correspond to bifurcations of ISPs and are, in some special cases, associated with changes in the Lagrangian structure of the flow (see, for example, §4.3 below).

It is worth emphasizing, however, that there is no general relationship between the (Eulerian) structure of ISPs in the time-dependent velocity field $\mathbf{v}$ and the Lagrangian structure of trajectories of the corresponding dynamical system (1). The paths of ISPs do not generally correspond to trajectories of the system (1) and they can often be eliminated by an appropriate coordinate transformation. Similarly, the instantaneous streamline patterns do not coincide with any invariant structures in the flow and attempts to determine transport properties from their geometry are generally inappropriate (unless the flow is steady or slowly varying). However, the paths of hyperbolic ISPs can be used as an initial guess in an iterative algorithm developed in [22] which identifies a class of *hyperbolic trajectories* of the system (1) which are important in transport considerations.

Finite-time, Distinguished Hyperbolic Trajectories (DHTs).

Let $\mathbf{x} = \boldsymbol{\gamma}(t)$ be a trajectory of the system (1) and consider a linearisation of the flow about $\boldsymbol{\gamma}$[4] in the form

$$\dot{\boldsymbol{\xi}} = \partial_{\mathbf{x}}\mathbf{v}(\boldsymbol{\gamma}(t), t)\,\boldsymbol{\xi}, \tag{4}$$

where $\boldsymbol{\xi} = \mathbf{x} - \boldsymbol{\gamma}$ and $\partial_{\mathbf{x}}\mathbf{v}(\boldsymbol{\gamma}(t), t)$ is the Jacobian of $\mathbf{v}(\mathbf{x}, t)$ evaluated at $\mathbf{x} = \boldsymbol{\gamma}(t)$.

We say that $\boldsymbol{\gamma}(t)$ is finite-time hyperbolic on the time interval $\mathcal{T} = [t_i,\ t_f]$ if the equation (4) has an *exponential dichotomy* on $\mathcal{T}$. Roughly speaking, this means that trajectories located sufficiently close to $\boldsymbol{\gamma}$ can separate at an exponential rate. Formally, the equation (4) has the exponential dichotomy on $\mathcal{T}$ if there exists a projection $\mathbf{P}$ ($\mathbf{P^2} = \mathbf{P}$), and positive constants K, L, α, and β such that:

$$\begin{aligned} |\mathbf{X}(t, t_i)\mathbf{P}\mathbf{X}^{-1}(s, t_i)| &\leqslant Ke^{-\alpha(t-s)}, \quad \text{for} \quad t \geqslant s, \quad t, s \in [t_i,\ t_f], \\ |\mathbf{X}(t, t_i)(\mathbf{Id} - \mathbf{P})\mathbf{X}^{-1}(s, t_i)| &\leqslant Le^{-\beta(s-t)}, \quad \text{for} \quad s \geqslant t, \quad t, s \in [t_i,\ t_f], \end{aligned} \tag{5}$$

where $\mathbf{X}$ is the fundamental solution matrix of the system (4) (see [22, 8, 21, 34] for more information).

Similarly to the infinite-time setting, hyperbolic trajectories in flows defined by (1) over a finite time interval are clustered into highly convoluted, connected sets in the extended phase space (x, y, t). When analysing the Lagrangian transport in such flows, it is important to identify the location of those trajectories in the hyperbolic structures which play a 'distinguished' role as their 'organising centres', determining the geometry of the whole hyprbolic structure, or at least the geometry of its connected subset. We refer to such trajectories as *Distinguished Hyperbolic Trajectories* (DHTs). The notion of what is meant by the term "distinguished" is discussed in more detail in [22, 30].

The DHTs cannot, generally, be found analytically and we use the algorithm developed in [22, 23] to locate them. We emphasise here that, although we often use carefully chosen hyperbolic paths of ISPs of (1) as initial guesses in this iterative procedure, any frozen-time-hyperbolic path in the flow (1) can be used as the input for the

[4]Dynamical systems theory can often suffer from a proliferation of notation that may tend to obscure understanding. In our setting hyperbolic trajectories are generally time dependent, and are denoted by $\boldsymbol{\gamma}$. However, in some cases denoting the specific time dependence is not necessary and for the sake of a less cumbersome notation we may simply denote it as $\boldsymbol{\gamma}$.

algorithm if it leads to its convergence (see [23]). Due to the fact that the flow given by (1) is only known for a finite time interval, no DHT can be determined uniquely (cf. [22]). Instead, there exist a small neighbourhood of hyperbolic trajectories in (x, y, t) which can serve as the distinguished ones. The volume of this neighbourhood shrinks with increasing length of the time interval. In this work our use of the term DHT is utilitarian in the sense that the finite-time hyperbolic trajectories, and their associated stable and unstable manifolds, that we identify are constructed with particle trajectories and they provide a description of the transport associated with the front-eddy system that leads to a precise spatio-temporal description of Lagrangian transport.

Finally, we want to point out that there is another consequence associated with the notion of finite-time hyperbolic trajectory that is important for Lagrangian transport– "bifurcation of DHTs". From the point of view of classical dynamical systems theory, this is a nonsensical phrase since hyperbolicity is defined over an infinite time interval (i.e. a trajectory is either hyperbolic or not hyperbolic) and the notion of bifurcation is associated with a "loss of hyperbolicity" (practically, as some external parameter is varied). In the setting of finite-time dynamical systems theory hyperbolicity is a notion that is specific to the chosen time interval (cf.(5)). If one applies (5) to a trajectory over a different time interval, then it may not be finite-time hyperbolic for that time interval. This leads to the notion of "bifurcation of finite-time hyperbolic trajectories" and we hope to address this problem in a future publication.

Stable and unstable manifolds of DHTs.

The usefulness of the notion of hyperbolicity in transport considerations comes from the fact that one can define stable and unstable manifolds of a hyperbolic trajectory in time-dependent flows in a way analogous to associating separatrix streamlines with saddle points in steady flows. In the case of flows defined for all time, a *stable manifold* of a hyperbolic trajectory $\boldsymbol{\gamma}$, denoted at the time instant t^* by $W^s_\gamma(t^*)$, is defined as a set of points such that trajectories passing through these points at $t = t^*$ will approach $\boldsymbol{\gamma}$ at an exponential rate as time goes to infinity. (It can be shown that for two dimensional incompressible flows such a set of points lies on a curve.) Consequently, an *unstable manifold* at time t^*, denoted by $W^u_\gamma(t^*)$, corresponds to a curve having the property that trajectories passing through any point on this curve at $t = t^*$ approach $\boldsymbol{\gamma}$ at an exponential rate as time goes to minus infinity.

In the case of flows whose evolution is known only over the time interval $\mathcal{T} = [t_i,\ t_f]$ the above definitions have to be modified. A finite-time stable manifold of the hyperbolic trajectory $\boldsymbol{\gamma}(t)$ contains all trajectories, say $\boldsymbol{x}^s(t)$, whose distance from $\boldsymbol{\gamma}$ is smaller than the initial separation, i.e. $|\boldsymbol{\gamma}(t)-\boldsymbol{x}^s(t)| < |\boldsymbol{\gamma}(t_i)-\boldsymbol{x}^s(t_i)|$ for $t \in (t_i,\ t_f]$. Similarly, a finite-time unstable manifold contains all trajectories $\boldsymbol{x}^u$ whose distance from $\boldsymbol{\gamma}$ is less than the final distance, i.e. $|\boldsymbol{\gamma}(t_f) - \boldsymbol{x}^s(t_f)| < |\boldsymbol{\gamma}(t) - \boldsymbol{x}^s(t)|$ for $t \in [t_i,\ t_f)$. As long as the time interval $\mathcal{T}$ is finite, these manifolds have a non-zero volume in the extended phase space (x, y, t).

The link between the two definitions (i.e. in the finite- or infinite-time setting), is revealed when considering a finite-time evolution of a flow defined for all time. Then, every infinite-time hyperbolic trajectory has the 'true' stable and unstable manifolds which are contained within their 'thick' finite-time counterparts. Moreover, all the material manifolds (i.e. manifolds composed of the flow trajectories) contained in the finite-time unstable manifold identified for $\mathcal{T} = [t_i,\ t_f]$ necessarily approach the 'true' unstable manifold when we consider the flow evolution past t_f. Similarly, all material manifolds contained in the finite-time stable manifold identified for $\mathcal{T} = [t_i,\ t_f]$ necessarily approach the 'true' stable manifold when considering the backward-time flow evolution past t_i. Of course, this 'asymptotic thinning' is not present for the

finite-time stable and unstable manifolds of trajectories which are only finite-time hyperbolic, even in flows defined for all time.

We note finally that in the finite-time setting any material manifold contained, for example, in the finite-time ustable manifold of a DHT can be used in transport considerations. This is because, from the point of view of transport, the 'invariance' property of a chosen material manifold is more important than its uniqueness, as long as this manifold is contained within the finite-time stable or unstable manifolds of the relevant DHT. As noted at the beginning of this section, the stable and unstable manifolds of DHTs provide an organising template for structure of other flow trajectories and they separate qualitatively different flow regions, thus serving as Lagrangian transport barriers (i.e. fluid cannot cross them by purely advective processes)[5]. In our work we compute these manifolds using the algorithms developed in [29, 31] and, when using the notion of the stable (or unstable) manifold hereafter, we mean a particular material manifold contained in the corresponding finite-time stable (or unstable) manifold.

Lobes

Lobes are formed from pieces of stable and unstable manifolds of hyperbolic trajectories. Their evolution can be used to understand the spatio-temporal mechanism for "long range transport" away from localized flow structures, and they can be used to explain how flow structures (such as a front and an eddy) "interact" from the point of view of Lagrangian transport. Here we recall the basic definitions of lobes, as well as some of their properties. However, more detailed discussion can be found in [27, 30, 40].

In contrast to steady two-dimensional flows, the stable and unstable manifolds of hyperbolic trajectories in time-dependent flows can intersect, at a fixed time instant, at isolated points within the flow domain. Consider one such point, say $\boldsymbol{p}_i$ at time $t = t_i$ (see figure 3), which lies on the intersection of an unstable manifold of a hyperbolic trajectory $\boldsymbol{\gamma_1}$, denoted at $t = t_i$ as $W^u_{\gamma_1}(t_i)$, and a stable manifold of a hyperbolic trajectory $\boldsymbol{\gamma_2}$, denoted as $W^s_{\gamma_2}(t_i)$ (note that homoclinic intersections are also allowed when $\boldsymbol{\gamma_1} = \boldsymbol{\gamma_2}$, as shown in figure 3). Then, one can construct a path connecting $\boldsymbol{p}_i$ and $\boldsymbol{\gamma_1}(t_i)$ along $W^u_{\gamma_1}(t_i)$, which we denote as $W^u_{\gamma_1}\{\boldsymbol{\gamma}_1(t_i), \boldsymbol{p}_i\}$[6], and another path connecting $\boldsymbol{p}_i$ and $\boldsymbol{\gamma_2}(t_i)$ along $W^s_{\gamma_2}(t_i)$, which we denote as $W^s_{\gamma_2}\{\boldsymbol{\gamma}_2(t_i), \boldsymbol{p}_i\}$. A particular subset of such intersection points, called *primary intersection points* ('pip'), turns out to play an important role in further constructions. Formally a primary intersection point (at the time instant $t = t_i$), of two invariant manifolds of hyperbolic trajectories is defined (see [27]), as a point that satisfies

$$W^u_{\gamma_1}\{\boldsymbol{\gamma}_1(t_i), \boldsymbol{p}_i\} \cap W^s_{\gamma_2}\{\boldsymbol{\gamma}_2(t_i), \boldsymbol{p}_i\} = \boldsymbol{p}_i, \tag{6}$$

i.e. it is the only intersection point of the two manifold segments defined above. Note that the invariance of these manifolds under the flow induced by (1) implies invariance of their intersections which must therefore coincide with some trajectories of (1). Thus, if $\boldsymbol{p}_i$ is a pip at $t = t_i$, its image at some later time, say $t = t_j$, must also be a pip given by $\boldsymbol{p}_j = \mathbf{x}(t_j; t_i, \boldsymbol{p}_i)$, where $\mathbf{x}(\cdot\,; t_i, p_i)$ represents a trajectory of (1) passing through p_i

[5]Diffusive processes do induce cross-barrier transport which, however, often take place on much longer time scales than the time scales associated with the dominant advective mechanisms. This is often the case in laminar and quasi-turbulent flows.

[6]The reader should be cautious here. While the notations $W^u_{\gamma_1}(t_i)$ and $W^u_{\gamma_1}\{\boldsymbol{\gamma}_1(t_i), \boldsymbol{p}_i\}$ appear similar here, they mean something quite different. The former denotes the unstable manifold of $\boldsymbol{\gamma}_1(t_i)$ and the latter denotes a finite piece of the unstable manifold of $\boldsymbol{\gamma}_1(t_i)$, starting at $\boldsymbol{\gamma}_1(t_i)$ and ending at $\boldsymbol{p}_i$.

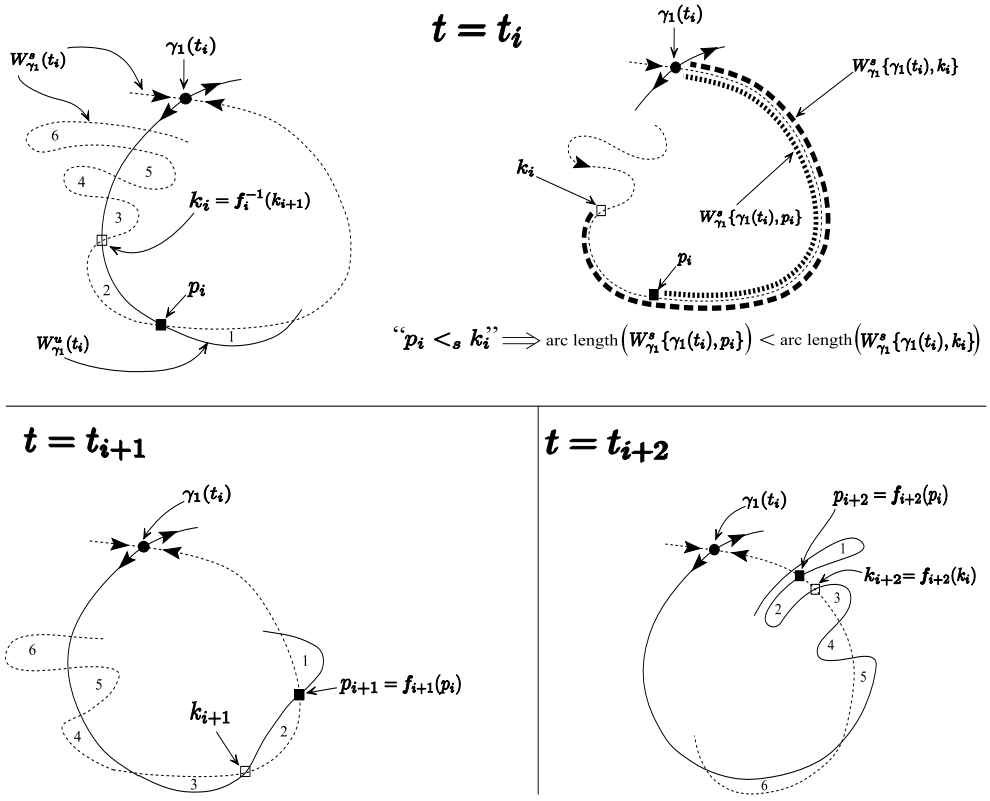

Figure 3: Maintenance of ordering of primary intersection points, $\boldsymbol{p}$ and $\boldsymbol{k}$, under flow evolution illustrated for three different times (t_i, t_{i+1}, t_{i+2}). The segment $W^s_{\gamma_1}\{\boldsymbol{\gamma_1(t), p(t)}\}$, connecting $\boldsymbol{\gamma_1}$ and $\boldsymbol{p}(t)$ along the stable manifold of $\boldsymbol{\gamma}_1$, is always shorter than the segment $W^s_{\gamma_1}\{\boldsymbol{\gamma_1(t), k(t)}\}$. The flow induced mapping, $\boldsymbol{f}$ (see (7)), maps the primary intersection points ('pips') along trajectories of the corresponding dynamical system. Note the evolution of lobes ("1", "2", "3", "4", "5", "6") associated with the boundary $\mathcal{B}(t)$ illustrated in figure 4.

at $t = t_i$. These relations can be cast in terms of a flow-induced mapping $\boldsymbol{f}$[7] between points on the same trajectory as (see also figure 3)

$$p_j = \boldsymbol{f}_j(p_i) \equiv \mathbf{x}(t_j; t_i, \boldsymbol{p}_i), \quad p_i = \boldsymbol{f}_i^{-1}(p_j) \equiv \mathbf{x}(t_i; t_j, \boldsymbol{p}_j). \tag{7}$$

Consider now two pips, $\boldsymbol{p}_i$ and $\boldsymbol{k}_i$ at time t_i, such that there are no other pips on the segments of $W^u_{\gamma_1}(t_i)$ and $W^s_{\gamma_2}(t_i)$ that connect $\boldsymbol{k}_i$ and $\boldsymbol{p}_i$. The invariance of these manifolds and their intersection points, $\boldsymbol{k}_i$ and $\boldsymbol{p}_i$, under the action of the flow induced mapping $\boldsymbol{f}$ implies that the region bounded at $t = t_i$ by the segments $W^u_{\gamma_1}\{\boldsymbol{k}_i, \boldsymbol{p}_i\}$ and $W^s_{\gamma_2}\{\boldsymbol{k}_i, \boldsymbol{p}_i\}$ is also invariant under the action of $\boldsymbol{f}$. We define a *lobe* as the area bounded by these manifold segments, and we denote it by $L^{k_i p_i}$ (see figure 3). If the flow given by (1) is incompressible (i.e. $\nabla \cdot \boldsymbol{v}) = 0$), the flow induced map $\boldsymbol{f}$ is volume-preserving and the area of the lobe remains constant throughout the evolution. A thorough discussion of *lobe dynamics* can be found in [38], [9], [43], [27]. Examples

[7]The notation $\boldsymbol{f}$ will serve to denote the mapping from one point to another along trajectories of the flow. A subscript, say i, on $\boldsymbol{f}$ will denote a specific time t_i at which initial points for the flow map are taken.

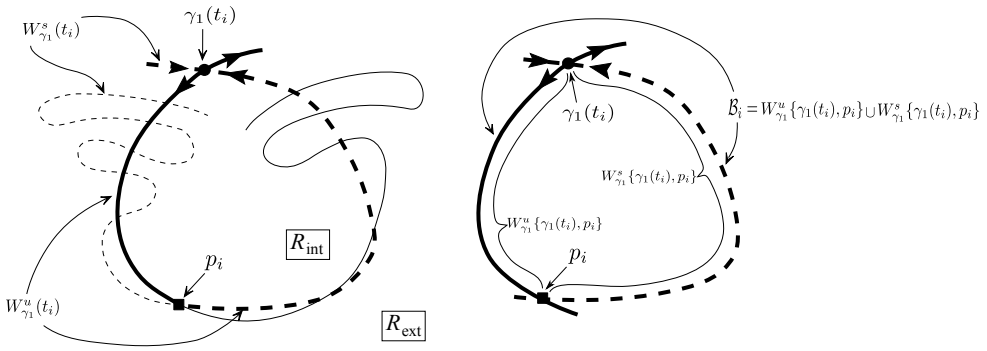

Figure 4: Schematic construction of a (time-dependent) boundary between two distinct regions R_{int} and R_{ext} in the case of a homoclinic manifold tangle of a hyperbolic trajectory γ_1. At the time instant $t = t_i$, the boundary $\mathcal{B}_i$ is made up of a segment of the unstable manifold $W^u_{\gamma_1}\{\boldsymbol{\gamma_1(t_i), p_i}\}$ and a segment of the stable manifold $W^s_{\gamma_1}\{\boldsymbol{\gamma_1(t_i), p_i}\}$ which intersect at the *boundary intersection point* $\boldsymbol{p}_i$.

of applications to oceanographic flows can be found in [35], [37], [45, 46].

The turnstile mechanism for transport.

Special lobes, called "turnstiles", are the mechanism for crossing a boundary constructed from stable and unstable manifolds of hyperbolic trajectories. The background and history of this notion can be found in [30] (relevant references for the original work for area-preserving maps are [6, 2, 26]). Here we describe the basics of the construction for aperiodic time-dependence and finite time given in [27, 40]).

For any primary intersection point, say $\boldsymbol{p}_{n-1}$ at some arbitrary time t_{n-1}, one can use the two segments of invariant manifolds, connecting $\boldsymbol{\gamma}_1(t_{n-1})$ to $\boldsymbol{p}_{n-1}$ along $W^s_{\gamma_1}(t_{n-1})$ and $\boldsymbol{\gamma}_2(t_{n-1})$ to $\boldsymbol{p}_{n-1}$ along $W^s_{\gamma_2}(t_{n-1})$, to define a Lagrangian barrier in the flow at $t = t_{n-1}$, as a continuous curve (see figure 4)

$$\mathcal{B}_{n-1} \;=\; W^u_{\gamma_1}\big\{\boldsymbol{\gamma}_1(t_{n-1}), \boldsymbol{p}_{n-1}\big\} \cup W^s_{\gamma_2}\big\{\boldsymbol{\gamma}_2(t_{n-1}), \boldsymbol{p}_{n-1}\big\}. \tag{8}$$

If we choose a monotonically increasing sequence of times $\{t_n\}$, $n \in \mathcal{I} \subset \mathbb{Z}$, and a corresponding sequence of pips $\{\boldsymbol{p}_n\}$, we can construct a family of barriers $\{\mathcal{B}_n\}$ for different times in the sequence $\{t_n\}$. In order to study transport across such a time-dependent boundary, one needs to be able to trace the evolution of lobes associated with it, which is facilitated via the turnstile mechanism. The turnstile lobes are constructed by first considering a sequence of pips $\{\boldsymbol{p}_n\}$ which additionally satisfy the *ordering under time evolution* in the form $\boldsymbol{p}_{n-1} <_s \boldsymbol{f}^{-1}_{n-1}(\boldsymbol{p}_n)$ (i.e. $\boldsymbol{p}_{n-1}$ is closer to $\boldsymbol{\gamma_2}(t_{n-1})$, in the sense of arc length along $W^s_{\gamma_2}(t_{n-1})$, than is $\boldsymbol{f}^{-1}_{n-1}(\boldsymbol{p}_n)$; see figure 3). Then, if there are N ($N \geqslant 0$) pips between endpoints of the segment $W^s_{\gamma_1}\big\{\boldsymbol{f}^{-1}_{n-1}(\boldsymbol{p}_n), \boldsymbol{p}_{n-1}\big\}$, there exist $N+1$ turnstile lobes associated with the boundary segment $\mathcal{B}_{n-1}$ which are delimited by the intersecting segments $W^u_{\gamma_1}\big\{\boldsymbol{f}^{-1}_{n-1}(\boldsymbol{p}_n), \boldsymbol{p}_{n-1}\big\}$ and $W^s_{\gamma_1}\big\{\boldsymbol{f}^{-1}_{n-1}(\boldsymbol{p}_n), \boldsymbol{p}_{n-1}\big\}$. As time evolves to $t = t_n$, such turnstile lobes are mapped under the flow action $\boldsymbol{f}$ to the lobes delimited by the intersecting segments $W^u_{\gamma_1}\big\{\boldsymbol{p}_n, \boldsymbol{f}_n(\boldsymbol{p}_{n-1})\big\}$ and $W^s_{\gamma_1}\big\{\boldsymbol{p}_n, \boldsymbol{f}_n(\boldsymbol{p}_{n-1})\big\}$. We will use this construction extensively in §4.1 and §4.2.

In our analysis of the Lagrangian transport associated with the interaction of the front and eddies the turnstile lobes will play a crucial role. In more detailed consid-

erations we will refer to "simple turnstile lobes" and "composite turnstile lobes". By *simple turnstile lobes* we essentially mean the turnstile lobes constructed above–at a given time the lobes defined by segments of stable and unstable manifolds between the boundary intersection point at that time and the pre-image of the boundary intersection point from the next observation time (and possibly the image of these turnstile lobes at the next observation time). By *composite turnstile lobes* we mean the manifold structure formed by the turnstile lobes at a given time and the intersection with evolution of turnstile lobes from earlier times. These phrases will be made clear by explicit examples relevant to the front-eddy interaction in later sections.

Working definition of a Lagrangian eddy.

Here we describe our working definition of a *Lagrangian eddy*. Identification of eddies, or vortices, in flows is a topic that has received a great deal of attention in the fluid dynamics literature; [19] contains a recent discussion of the issues as well as a survey of the literature (but see also [36, 3, 10, 17, 24]). We seek a "working definition" of a Lagrangian eddy which will enable us to determine when such an eddy is present and the manner in which fluid is entrained and detrained by the eddy. For our purposes, and in line with our usage of hyperbolic trajectories and their stable and unstable manifolds for constructing Lagrangian flow structures, a Lagrangian eddy will be a region bounded by intersecting segments of stable and unstable manifolds of hyperbolic trajectories with the resulting swirling sense of motion (clockwise or anticlockwise) on the boundary induced by the motion of trajectories making up the boundary segments. This construction of an eddy was used earlier in [20], where the name *dynamic eddy* was proposed, and in [30] to describe the Lagrangian transport associated with the interaction of an eddy with a jet. Figure 4 is an example of a Lagrangian eddy constructed in this way using one hyperbolic trajectory where the motion on the boundary is in the counterclockwise sense. The relevant turnstile lobes, associated with the eddy boundary, can be constructed in the way described earlier and the resulting evolution of the turnstile lobes can be used to analyse the entrainment and detrainment of fluid from the eddy, as well as the detailed motion of fluid inside the eddy. We remark that most procedures that identify eddies in the recent oceanographic data sets are Eulerian in nature, e.g. [7] uses the Okubo-Weiss criteria. It is an interesting question to relate our Lagrangian construction of an eddy and the other criteria described above. However, this is an extensive research topic in its own right and well beyond the scope of this paper.

4 Lagrangian structures and transport in the front-eddy system

Transport across an oceanic front, identified in the North-Western Mediterranean Sea, was recently discussed in detail in [28]. The authors pointed out there that the presence of strong eddies near the studied (Lagrangian) front could open up new transport routes and, consequently, introduce additional complexity to transport processes acting near the front, especially when following the flow evolution over time intervals longer than those considered in [28]. In the previously discussed flow configuration it sufficed to identify a tangle of two invariant manifolds of two DHTs located at the two ends of the front and use them to define a Lagrangian barrier between two disjoint regions of the flow domain as well as a set of turnstile lobes mediating transport across the front. In order to take into account the existence of the additional long-lived, localised

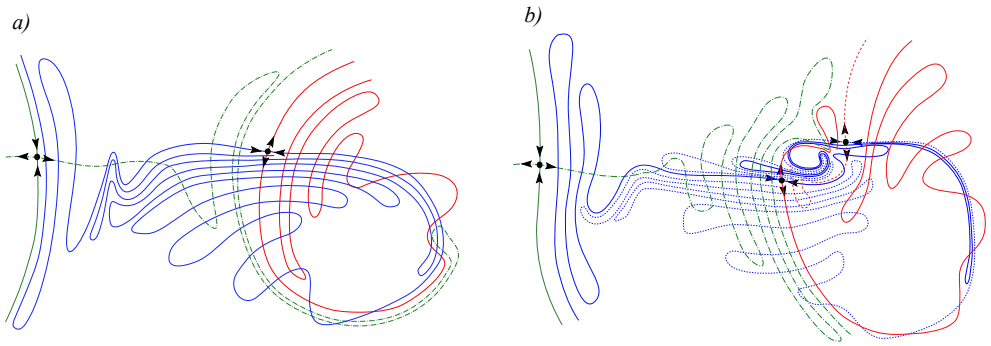

Figure 5: Sketch of possible geometry of the stable and unstable manifolds of the Distinguished Hyperbolic Trajectories (DHTs) in a flow characterised by a meandering westerly current which interacts with an eddy (a) or an eddy pair (b). Segments of these manifolds are necessary to define turnstile lobes which mediate transport between different regions in the flow (compare (a) with figures 6b, 7b, 10 and (b) with figures 13a, 14a). Note that different number of DHTs (and manifolds) is present in the two cases.

flow structures, potentially interacting with the front, we now have to consider much more complicated manifold structures. We focus here on two different situations which involve an interaction of a Lagrangian front with one or two Lagrangian eddies. We refer to these two cases as, respectively, Scenario I and Scenario II. Such a choice was largely motivated by a careful inspection of the realistic flow data obtained for the North-Western Mediterranean Sea from the DieCAST model, already mentioned in §2.

As a 'visual' introduction to the complexity of the problem we present in figure 5 two sketches showing snapshots of possible manifold geometry associated with the two scenarios. Since the underlying flow field is time-dependent, these manifold tangles evolve in time subject to certain topological constraints and, in particular, it is possible for the manifold structure to evolve between the configurations of Scenario I and II. Our analysis develops methods for understanding the essential features and basic building blocks that generate this complex spatio-temporal structure and its influence on Lagrangian transport.

Our goal in this section is two-fold. First, we aim to understand transport processes acting in Scenarios I and II and, in particular, the effects of the intermittent transitions between these scenarios on transport. We also want to outline a general procedure for extracting the relevant Lagrangian information from the Eulerian velocity data associated with complex, time-dependent flows.

We note finally that, although we consider here a system in which the Lagrangian front interacts with the eddy (or the eddy pair), situations in which these Lagrangian structures do not interact are also possible. We give an example of such a situation in §5 where, despite a presence of a meandering current and a collection of time-dependent Eulerian eddies, the corresponding Lagrangian structures do not interact.

4.1 Transport associated with the interaction of an Eulerian current with a single eddy

The Eulerian flow features which are often associated with the existence of the Lagrangian flow structure of Scenario I (see figure 5a) were highlighted earlier in figure 1.

It is generally impossible to predict with certainty that such a Lagrangian structure exists in a flow until the geometry of the relevant invariant manifolds is determined. As can be seen in figure 5a, the manifolds in the tangle we associated with Scenario I belong to two DHTs (cf. §3.1) which we refer to hereafter as the western DHT ($\mathcal{H}_W$) and the eastern DHT ($\mathcal{H}_E$). It is thus necessary that we first demonstrate the existence of these 'special' hyperbolic trajectories in the flow. This is not always a straightforward task, since we search for these DHTs using an iterative algorithm, described in [22], which requires a 'good' initial guess in order to converge. In the search process, we are usually guided by the Eulerian flow features, such as the hyperbolic ISPs, which remain near the ends, or near branching points, of the identified current. We usually use such paths of ISPs as the initial guesses in the DHT-finding algorithm. However, we remind the reader that any other frozen-time hyperbolic guess could be used in the algorithm, as long as it leads to its convergence to a hyperbolic trajectory (see §3.1 and [23]).

Assuming that we located the required DHTs in the flow and computed sufficiently long segments of their (time-dependent) stable and unstable manifolds, we can analyse the Lagrangian transport processes associated with Scenario I, using the tools introduced in §3.1. In order to do that, we first need to identify the geometry of a (time-dependent) boundary between different regions present in the flow for an ordered sequence of 'observation times' $t_0 < t_1 < ... < t_N$. Here, we choose only a two element sequence $\{t_1, t_2\}$, which is sufficient to illustrate the construction of the boundary, as shown in figure 6, and to understand the action of the turnstile mechanism which mediates transport across different parts of this boundary.

Construction of the boundary segment $\mathcal{B}^{I-II}$ coincides with that presented in [28] and relies on the fact that, generically, invariant manifolds of DHTs in unsteady flows intersect repeatedly (but this must be verified for specific data sets). This allows us to choose a sequence of boundary intersection points $\{bf_i\}$ (see §3.1 and figures 3, 4), one for each time t_i, and define $\mathcal{B}_i^{I-II}$ as the union of the segment $W^u_{\mathcal{H}_W}\{\mathcal{H}_W, bf_{t_i}\}$ of the unstable manifold of $\mathcal{H}_W$ and of the segment $W^s_{\mathcal{H}_E}\{\mathcal{H}_E, bf_{t_i}\}$ of the stable manifold of $\mathcal{H}_E$ (cf. (8)). Hereafter, we refer to the segment $\mathcal{B}^{I-II}$ as the 'front', since its location is correlated with sharp gradients of salinity and temperature fields in the data (see [28]).

In order to capture additional transport features associated with the existence of the Lagrangian eddy at the eastern end of the front, we also have to take into account the geometry of the remaining branches of invariant manifolds of $\mathcal{H}_E$. The boundary between the eddy region and the surrounding flow at $t = t_i$, denoted as $\mathcal{B}_i^{II-III}$, is given by the union of two segments of invariant manifolds associated with $\mathcal{H}_E$: a segment of its unstable manifold, $W^u_{\mathcal{H}_E}\{\mathcal{H}_E, be_{t_i}\}$, and a segment of its stable manifold, $W^s_{\mathcal{H}_E}\{\mathcal{H}_E, be_{t_i}\}$, intersecting at the boundary intersection point be_{t_i} (see figure 6).

Consequently, at any time instant, we can distinguish three distinct regions in the flow domain, which are separated by Lagrangian barriers formed by the connected boundary segments $\mathcal{B}^{I-II}$ and $\mathcal{B}^{II-III}$. We denote the region to the North of the front by R_I, the interior of the eddy by R_{III}, and the region bordering the eddy from the South and the North-East by R_{II}. The analysis of transport between these regions requires different levels of complexity, depending on the transport route considered. In order to understand transport processes across the front or across the eddy boundary (i.e. the routes of the form $R_i \leftrightarrow R_j$), it is sufficient to analyse the evolution of simple turnstile lobes associated with the respective boundary segment (see figure 7). Understanding transport routes which arise due to the interaction between the front and the eddy requires taking into account those pairs of simple turnstile lobes, as-

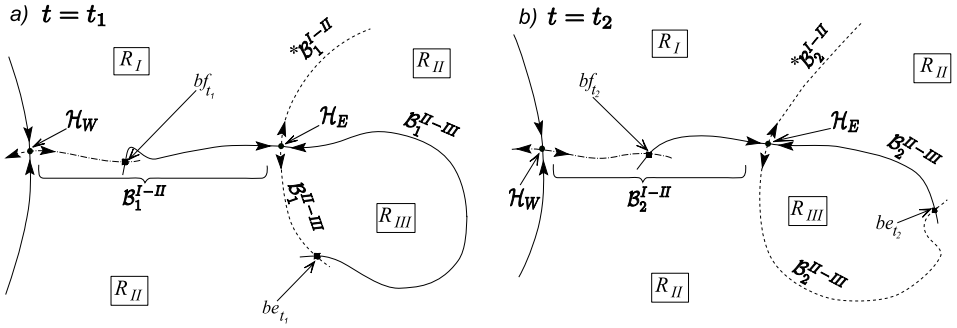

Figure 6: **Scenario I**. Construction of a time-dependent boundary, $\mathcal{B}^{I-III} \cup \mathcal{B}^{II-III}$, which involves invariant manifolds of two hyperbolic trajectories $\mathcal{H}_W$ and $\mathcal{H}_E$. The geometry at two 'observation' times (a) $t = t_1$ and (b) $t = t_2$ ($t_2 > t_1$) is sketched. We show only the manifold segments which are necessary to define the boundary at a given time. The intersection points of invariant manifolds used in the construction of the boundary (i.e. boundary intersection points) are denoted by bf_{t_1} and bf_{t_2} for the front, and by be_{t_1}, be_{t_2} for the eddy. The boundary divides the flow domain into three distinct regions: R_I, R_{II} and R_{III}.

sociated with the front and the eddy boundary, which overlap with each other (see figure 10, 12). Finally, there are transport processes whose understanding requires the existence of the composite turnstile lobes in the underlying flow. Below, we discuss transport routes present in Scenario I and shown schematically in figure 18a in the order of increasing complexity.

Transport across the front ($R_I \leftrightarrow R_{II}$)

The turnstile lobes associated with the front ($\mathcal{B}^{I-II}$) can be constructed in a standard way which was carried out earlier in [28]. We do so by considering the lobes formed at $t = t_1$ by the intersecting segments of $W^u_{\mathcal{H}_W}$ and $W^s_{\mathcal{H}_E}$ between two *primary intersection points*, bf_{t_1} and $bf^-_{t_2}$ (see figure 7), which satisfy the ordering under the flow evolution in the form $bf_{t_1} <_s bf^-_{t_2}$ (see figure 3). The point bf_{t_1} is the boundary intersection point at $t = t_1$ and the point $bf^-_{t_2}$ denotes the pre-image of the boundary intersection point at $t = t_2$ under the the volume- and orientation-preserving map $\boldsymbol{f}$ (cf. (7)), induced by the underlying flow (i.e. $bf^-_{t_2} \equiv \boldsymbol{f}^{-1}_{t_1}(bf_{t_2})$). An example of a two-lobe front turnstile constructed in this way is shown in figure 7a (see the lobes marked by "□" and "△"). Provided that the next observation time t_2 is chosen in such a way that the turnstile is advected sufficiently close to $\mathcal{H}_E$, under the action of $\boldsymbol{f}$, the two front lobes must evolve in the way shown in figure 7b which results in a transfer of fluid particles confined within these lobes across the front.

In order to show the existence of such a transport route in the aforementioned flow in the North-Western Medirranean Sea (cf. §2), we show in figure 8 the computed geometry of the relevant invariant manifolds in the flow at day 664 and day 683. The blue curves mark there the stable manifold of the eastern DHT ($\mathcal{H}_E$) and the red curve denotes the unstable manifold of the western DHT ($\mathcal{H}_W$). The two sets of coloured dots mark locations of a fixed number of conveniently chosen fluid-particle trajectories at the two time instants, and are to aid the visualisation of transport across the front. The magenta-coloured dots mark fluid particles confined to northern lobes, i.e. the lobes originating close to $W^s_{\mathcal{H}_W}$ north of the front segment $\mathcal{B}^{I-II}$ in figure 8a). The green-coloured dots mark fluid particles confined to southern lobes (i.e. the lobes originating close to $W^s_{\mathcal{H}_W}$ south of the front on day 664). At the later stage of the

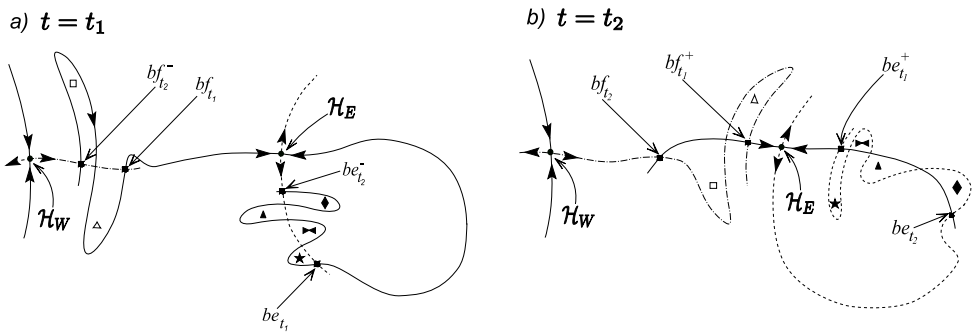

Figure 7: **Scenario I**. Schematic construction of turnstile lobes for the front and the eddy at (a) $t = t_1$ and their geometry after evolution to $t = t_2$ (b) (see also figure 6). The front turnstile lobes are defined as the lobes formed by segments of $W^u_{\mathcal{H}_W}$ and of $W^s_{\mathcal{H}_E}$ between the boundary intersection point ('*bip*') at $t = t_1$, denoted as bf_{t_1}, and the pre-image of the *bip* at $t = t_2$, denoted by $bf^-_{t_2} \equiv \boldsymbol{f}^{-1}_{t_1}(bf_{t_2})$. At $t = t_2$, bf_{t_1} evolves to $bf^+_{t_1} \equiv \boldsymbol{f}_{t_2}(bf_{t_1})$. The action of the flow-induced mapping $\boldsymbol{f}$, defined by (7), was illustrated in figure 3. The eddy multilobe turnstile, bounded by $be^-_{t_2}$ and be_{t_1} at $t = t_1$ is constructed in an analogous way. The squares, triangles and stars are to aid visualization of how the turnstile lobes evolve from t_1 to t_2.

evolution, shown in figure 8b, the northern lobes containing the magenta dots end up south of the front and the southern lobes containing the green dots have migrated to the north of the front by day 683.

Transport in and out of the eddy ($R_{II} \leftrightarrow R_{III}$)

The basic transport mechanism across the boundary of the eddy region ($\mathcal{B}^{II-III}$) can be described in a way analogous to the one developed for the transport across the front although, in this case, the existence of homoclinic tangles (rather than heteroclinic tangles) is needed for transport across this boundary segment to take place. We note here that this transport route is also present in Scenario II and it remains active even if the flow structure evolves intermittently between Scenarios I and II. We construct the relevant simple turnstile lobes by considering the lobes formed by the intersecting segments of $W^u_{\mathcal{H}_E}$ and $W^s_{\mathcal{H}_E}$ between the pre-image of the *bip* at $t = t_2$, denoted as $bf^-_{t_2} = f^{-1}_{t_1}(bf_{t_2})$, and the boundary intersection point bf_{t_1} (see the lobes marked by ▲, ★, ⋈, ♦ in figure 7). The evolution of such lobes is governed, as before, by the volume- and orientation-preserving map $\boldsymbol{f}$ induced by the flow. The invariance of the manifold intersection points under the action of $\boldsymbol{f}$ implies that at $t = t_2$ these lobes are bounded by the segments of invariant manifolds between bf_{t_2} and $bf^+_{t_1} = \boldsymbol{f}_{t_2}(bf_{t_1})$, as shown in figure 7b.

Assuming that the relevant Lagrangian flow structure is fully captured by Scenario I (i.e. there are no intersections between $\mathcal{B}^{II-III}$ and stable or unstable manifolds of other DHTs), the eddy turnstile lobes are advected away from $\mathcal{H}_E$ in a counter-clockwise sense around the perimeter of the large eddy region R_{III} until they re-approach $\mathcal{H}_E$ along $W^s_{\mathcal{H}_E}$. By then, the eddy lobes which were initially located in R_{II} (see ▲, ★) are entrained into the eddy region and the lobes which originated inside the eddy at $t = t_1$ (see ⋈, ♦) are ejected to R_{II} and stretched into long filaments along the unstable manifold of $\mathcal{H}_E$ (see figure 7b).

Note also that fluid particles located south of the front at $t = t_1$ (in the region R_{II}) but not contained in the eddy lobes will travel around the perimeter of the eddy region

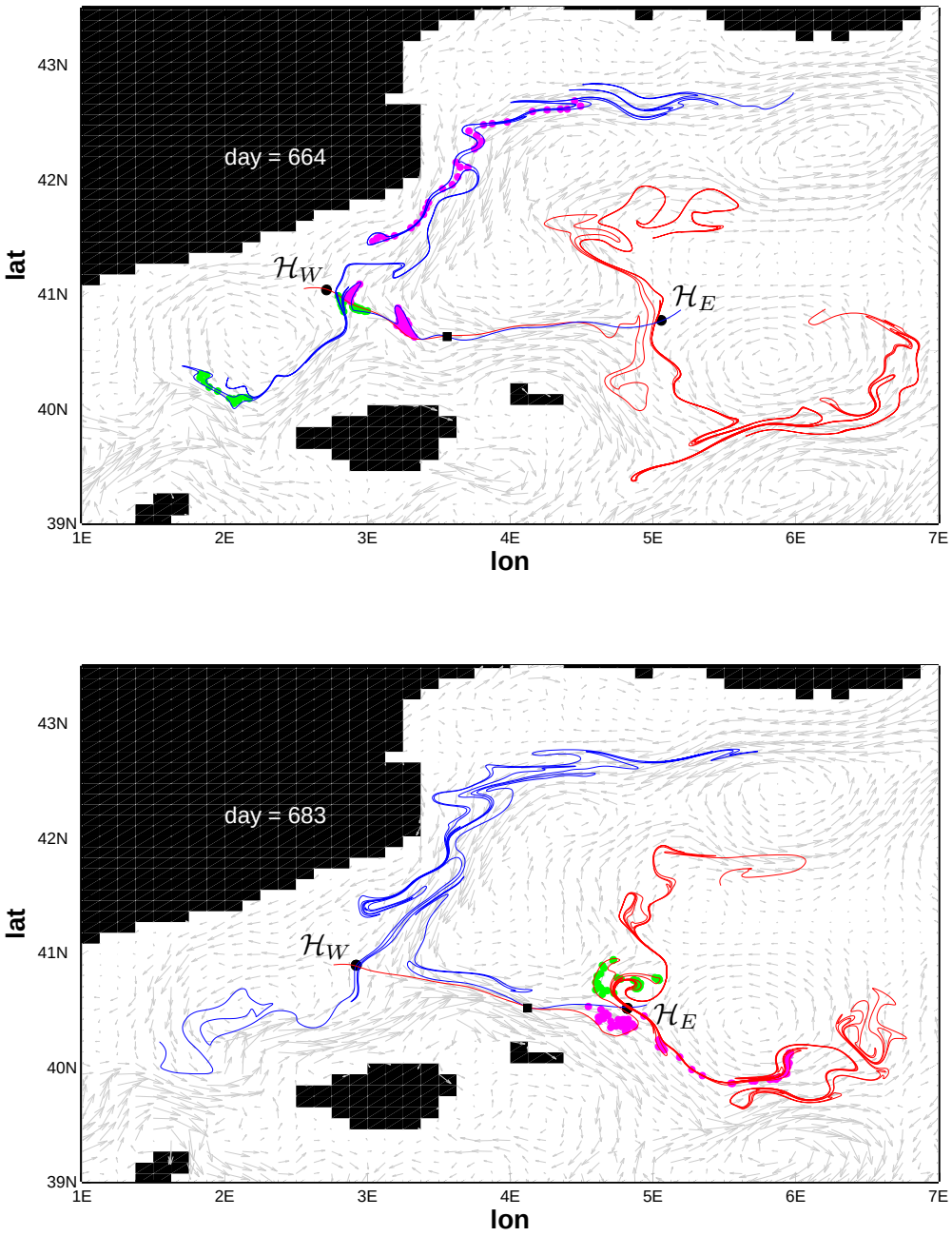

Figure 8: **DieCAST model, NW Mediterranean.** Transport across the Lagrangian front (see the segment $\mathcal{B}^{I-II}$ in figures 6, 13) between days 664 and 683 illustrated by following the evolution of a set of trajectories which originate in lobes located initially to the South of the front (green; region R_{II}) and in lobes to the North of the front (magenta; region R_I). This transport route acts in the way sketched in figures 7 and 14 (see the lobes □, △).

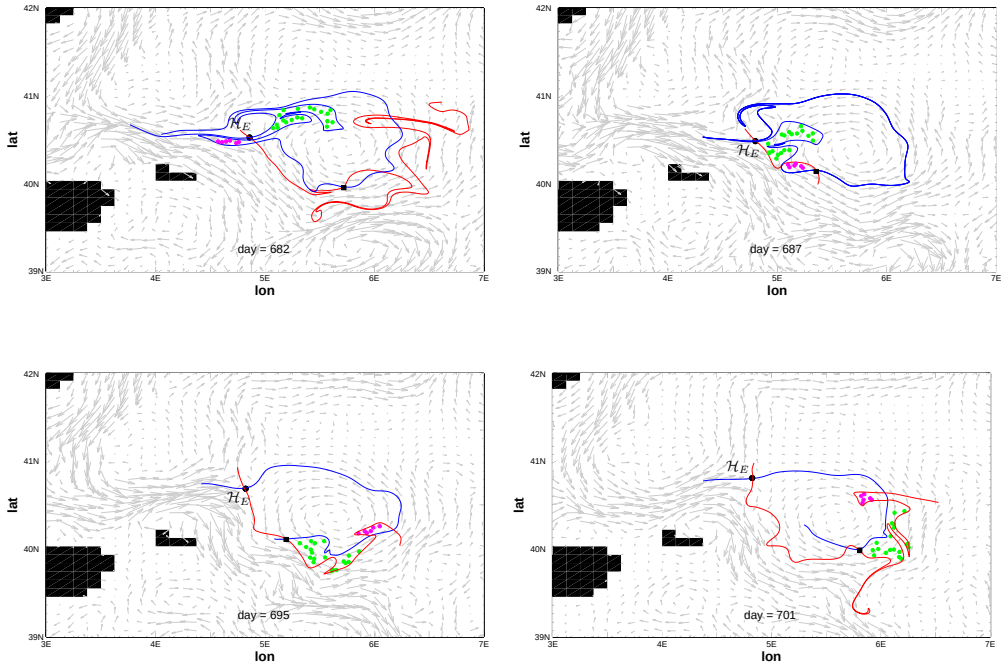

Figure 9: **DieCAST model, NW Mediterranean.** Transport across the eddy boundary (segment $\mathcal{B}^{II-III}$ in figures 6, 13) between days 682 and 701 illustrated using a two-lobe turnstile (compare with figure 7). The red and blue curves mark, respectively, the unstable and stable manifolds of the hyperbolic trajectory denoted by the black dot. The black squares denote the boundary intersection points.

without being entrained into R_{III}, and then proceed to the North along the unstable manifold of $\mathcal{H}_E$. This transport route is sketched in figure 18 as the outermost blue path, located outside R_{III} (note that this route is also present in Scenario II). Whether a fluid particle is advected around exterior of the eddy to the North, or whether it is entrained first into the eddy region and rapidly stirred before exiting to the North is very sensitive to the spatial and temporal location of the particle (i.e. it depends on which lobe it is in).

We now illustrate this transport route in the same front-eddy system which we identified earlier in the North-Western Mediterranean Sea (figures 1, 2), and which we used to illustrate the transport across the front (figure 8). We note that within the time intervals required to observe the turnstile transport mechanism across the eddy boundary the Lagrangian flow structure often evolves intermittently between Scenarios I and II. However, as can be seen from our construction shown in figures 7 and 14, the short-term transport across the boundary segment $\mathcal{B}^{II-III}$ remains unchanged regardless of whether the flow evolves according to Scenario I or Scenario II. We discuss the effect of this transitions on transport in more details in §4.3.

Figure 9 shows the computed geometry of the relevant invariant manifolds of $\mathcal{H}_E$ whose segments make up the large, time-dependent eddy region at the eastern end of the front (see R_{III} in figures 6, 13). The four snapshots shown in the insets correspond to days 682, 687, 695 and 701 in the simulation. The boundary intersection point at each of these times is marked by the black square and the stable and unstable

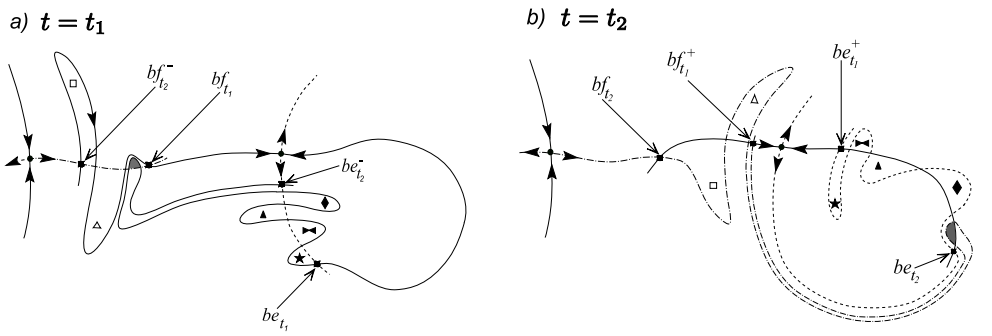

Figure 10: **Scenario I**. Illustration of an interaction between the front lobes and the eddy lobes (note that the *bip* at t_1 (i.e. bf_{t_1}) is defined differently to that of figure 6 in order to visualise the interaction). (a) initial geometry showing a lobe associated with the eddy boundary (i.e. $\mathcal{B}^{II-III}$ in figure 6) overlapping with one of the lobes associated with the front; (b) the overlap area (shaded) is entrained into the eddy by $t = t_2$ (the eddy boundary at t_2 is defined in Fig. 6b).

manifolds of $\mathcal{H}_E$ are colour-coded in the same fashion as in figure 8 (i.e. red - the unstable manifold, blue the stable manifold). We highlight in this figure an evolution of a two-lobe turnstile associated with the eddy boundary $\mathcal{B}^{II-III}$ (see figure 6) by using the green- and magenta-coloured dots to mark locations of a fixed set of fluid particles. The green-coloured particles are confined within a lobe which initially, on day 682, was located inside R_{III}. These particles are expelled from the eddy region around day 695, as illustrated in figure 9c. At the same time, the fluid particles (magenta) confined within the eddy turnstile lobe located initially (day 682, figure 9a) in R_{II} are entrained into R_{III}, as shown in figure 9c,d.

Note that the transport processes responsible mass exchange across the Lagrangian front and across the boundary of the Lagrangian eddy would persist if we considered each of these flow structures in isolation. However, if the two structures interact with each other, additional transport routes open up in the flow, leading to enhanced tracer stirring in the combined system. We discuss these additional transport routes below.

Transport routes arising due to front-eddy interaction *($R_I \to R_{II} \to R_{III}$)*

The simple-turnstile mechanism outlined above is not capable of describing transport processes arising through the interaction of the front end the eddy. In order to determine whether or not a fluid (or tracer) particle which crossed the front from the North in a front lobe is subsequently going to be entrained into the large eddy region, one has to determine if this particle is also contained in one of the lobes associated with the eddy. Such a procedure usually requires examining simple turnstile lobes which have much larger arc lengths than those considered before. The necessary condition for an interaction between two distinct Lagrangian structures, which is manifested by mass transport across their respective boundaries, is the overlap between at least one pair of lobes belonging to each of these structures. In other words, we say that two (localised) Lagrangian flow structures, say A and B, interact if at least one lobe associated with A intersects at least one lobe associated with B. The invariance of the manifold intersection points under the flow induced map $\boldsymbol{f}$ implies then that a tracer captured within the intersecting area remains confined within it for all time (assuming no diffusion), which results in an entrainment of the intersecting part of the

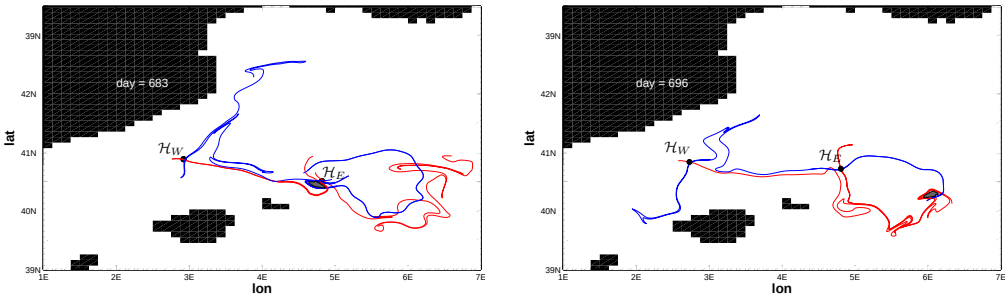

Figure 11: **DieCAST model, NW Mediterranean.** Interaction of the Lagrangian front with the large eddy manifested by an intersection of a front turnstile lobe with an eddy lobe (shaded area). Water contained within the intersecting area can be traced back to cold water lobes which originate in the North (see the magenta dots with figure 8 and the "□"-lobe in figures 7, 14). This volume of water is entrained into the large eddy across the boundary segment $\mathcal{B}^{II-III}$ inside a simple eddy lobe, according to the mechanism shown in figures 7, 14.

lobe associated with A inside B or vice versa. We note that this phenomenon has been observed before, for example in [30], although it was not explicitly defined.

In order to illustrate the interaction between a northern front lobe (i.e. a lobe associated with $\mathcal{B}^{I-II}$ which originates in R_I) and an eddy turnstile lobe, we change the location (with respect to that of figure 6a) of the boundary intersection points, bf_{t_1} and be_{t_1}, as shown in figure 10a. As a consequence, one of the lobes in the eddy turnstile now stretches over distances comparable with the characteristic length of the front and intersects with one of the front turnstile lobes (shaded area). Evolution of these turnstiles to $t = t_2$ results in the entrainment of a portion of the front lobe into the eddy region (see figure 10b). Note that only the northern lobes, i.e. the lobes that can be inverse-mapped to R_I using $\boldsymbol{f}$ (cf. 7), can be entrained into the eddy region R_{III} during such a process.

In [28] the turnstile mechanism for cross-frontal transport generates filaments of cold and less salty water protruding into the warmer and saltier region South of the front. If the geometry of the relevant manifolds is such that the eddy turnstile lobes intersect with the front turnstile lobes, as sketched earlier in figure 10, the flow evolution will first bring the cold-water, northern front lobe, containing the intersecting area, South of the front (to region R_{II}) and then into the large eddy. Such a scenario is indeed observed in the front-eddy system we identified in the North-Western Mediterranean Sea. We illustrate this process in figure 11 where the shaded area can be traced back in time to one of the lobes originating in the North (see figures 8 and 10).

Long-term transport associated with a Lagrangian eddy ($R_{II} \to R_{III} \to R_{II}$)

When analyzing the evolution of the simple lobes associated with the eddy region, i.e. the lobes ▲, ★, ⋈ and ♦ in figure 7, we showed how fluid particles can be entrained (inside the lobes ▲ and ★) into the eddy or ejected from its interior (inside the lobes ⋈ and ♦) across the boundary segment $\mathcal{B}^{II-III}$. However, while these essentially short-term mechanisms are much more likely to be important in flows where diffusive effects are important, they do not give any insight as to the redistribution of the entrained volume inside the eddy region and its subsequent ejection back to the outer flow. We

note that, it has been shown earlier (cf. [38, 39]) that in the case of incompressible, time-periodic flows a volume of fluid entering the eddy region must eventually leave it. The analogous situation in arbitrary time-dependent flows has not, however, been analysed in the same manner. We illustrate such a process in figure 12 for the simplest possible manifold geometry. We show there a sequence of snapshots which reveal the instantaneous geometry of a number of evolving complex lobes which are formed by relatively long, intersecting segments of the stable and unstable manifolds of a hyperbolic trajectory $\mathcal{H}_E$. The time-dependent eddy region is defined by the thick manifold segments with the boundary intersection point denoted (for each time) by a black square. The lobe evolution is governed by the orientation- and volume-preserving map $\boldsymbol{f}$ induced by the underlying flow (see (7) and figure 3). For clarity, we drop the volume preservation of $\boldsymbol{f}$ in the sketches, while retaining the essential 'topological' features of the evolution reflected in the invariance of the manifold intersection points and the preservation of their ordering (see also figure 3) under the flow evolution. As it turns out, a volume of fluid can be first entrained and then subsequently ejected from the (time-dependent) eddy region, only if it remains outside of both the blue and the red shaded regions indicted in each inset of figure 12. The boundaries of these two regions are determined (for the most part) by, respectively, the stable and the unstable manifolds of $\mathcal{H}_E$. We illustrate the transport route, denoted symbolically as $R_{II} \rightarrow R_{III} \rightarrow R_{II}$, by following the evolution of a volume of fluid marked by the green shaded area in the insets of figure 12, which is confined within a *composite lobe* (i.e. a simple lobe with internal structure taken into account, see §3.1). One can immediately notice that considering the evolution of the composite lobes introduces additional complexity when compared to the simple turnstile mechanism discussed earlier. However, only for such a complex manifold configuration can the 'topologically' constrained evolution of the relevant lobes result in an entrainment and a subsequent ejection of the fluid volume from the eddy region. In the simplest scenario shown here, after (roughly) one revolution around the perimeter of the boundary, the green portion of the entrained fluid is transferred into a portion of a lobe located in the interior of the eddy region (i.e. the lobe formed by the segment of $W^s_{\mathcal{H}_E}$ intersecting the red boundary segment figure 12d). This lobe is subsequently ejected to the outer flow (figure 12d-f), just like the lobe "⋈" in the process illustrated earlier in figure 7.

4.2 Additional transport routes associated with the emergence of the second eddy in the front-eddy system

The evolution of the velocity field obtained from the DieCAST ocean circulation model (cf. §2) for the North-Western Mediterranean Sea is characterised by an intermittent emergence and disappearance of an additional smaller Eulerian eddy at the eastern end of the front, as illustrated earlier in figures 1 and 2. The evolution of the associated temperature field indicates that the presence of the second Eulerian eddy is often correlated with an injection of warm-water filaments into the large eddy region from the North, across the small eddy, and that such a process is not present when the small eddy disappears. The appearance of this additional transport route indicates indirectly a change in the underlying Lagrangian flow structure with respect to Scenario I (cf. figure 5b) where such a transport process cannot be realised. We develop here the Lagrangian characterisation of a front-eddy system which is composed of two Lagrangian eddies interacting with the front. We refer to such a flow geometry as Scenario II and describe the Lagrangian mechanism responsible for the entrainment of warm water filaments into the large eddy region across the small eddy region. We

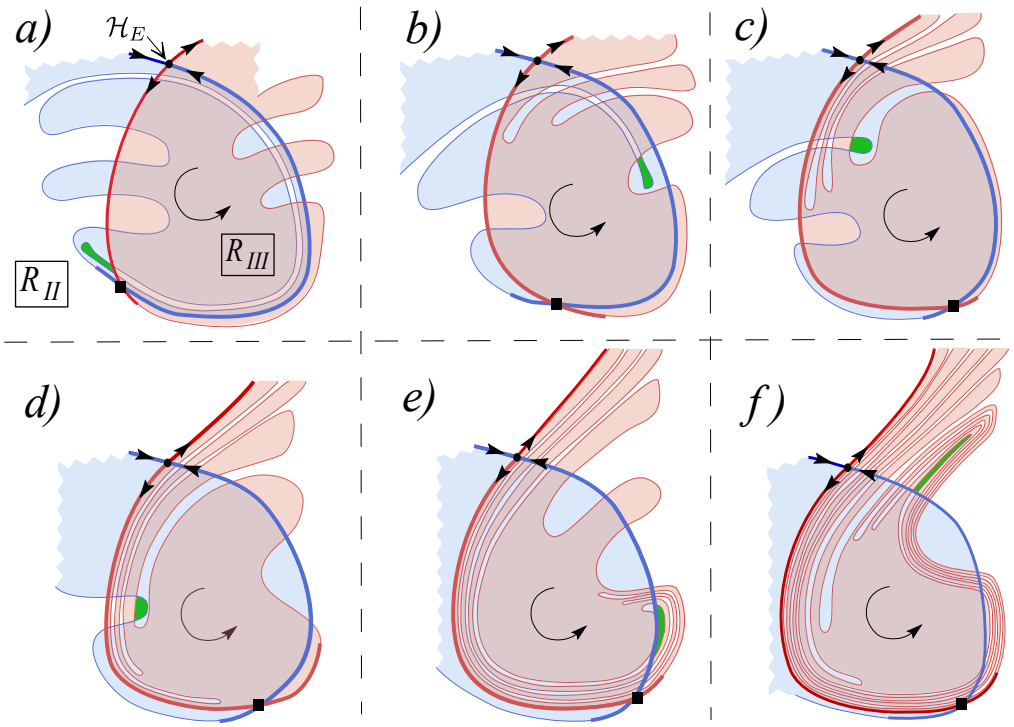

Figure 12: **Scenario I**. Illustration of an entrainment of fluid, located initially inside the green lobe in region R_{II}, into the eddy region, R_{III}, and its subsequent ejection at a later time back to R_{II} along the unstable manifold of $\mathcal{H}_E$. The simplest possible geometry of relevant invariant manifolds is shown here and the incompressibility of the underlying flow is not preserved in order to aid visualisation. This complex process cannot be explained using the 'simple' lobes used in figure 7. Depending on the actual flow field, this process may be terminated prematurely if the Lagrangian flow structure changes or if it is significantly affected by diffusion.

later show, in §4.3, show how these two Lagrangian structures (i.e. Scenario I and II) can evolve between each other.

The emergence of the additional Eulerian eddy at the end of the front is accompanied by a saddle-node bifurcation of the ISP path which was earlier used to locate $\mathcal{H}_E$ in §4.1. This bifurcation produces an elliptic ISP, which we associate with the birth of the new Eulerian eddy, and a new hyperbolic ISP. The newly created path of the hyperbolic ISPs can be used as an initial guess in the DHT-finding algorithm [22] in an attempt to determine whether a new DHT exists in the flow, alongside the previously located DHTs which enabled us to recognise the manifold geometry of Scenario I. If such a procedure does indeed lead to the identification of the additional DHT, the underlying structure of the intersecting invariant manifolds of the three DHTs forms a tangle which is rather different than the one associated with the Lagrangian geometry of Scenario I (see figure 5b).

In what follows, we will denote the DHT on the western end of the front as $\mathcal{H}_W$, as in the description of Scenario I, and the two remaining DHTs by $\mathcal{H}_{NE}$ and $\mathcal{H}_{SW}$, according to their relative geographical location (see figures 5b and 13). For this geometry, in addition to the previously identified disjoint regions in the flow domain, R_I, R_{II} and R_{III}, we can distinguish the fourth region, denoted as R_{IV}, corresponding

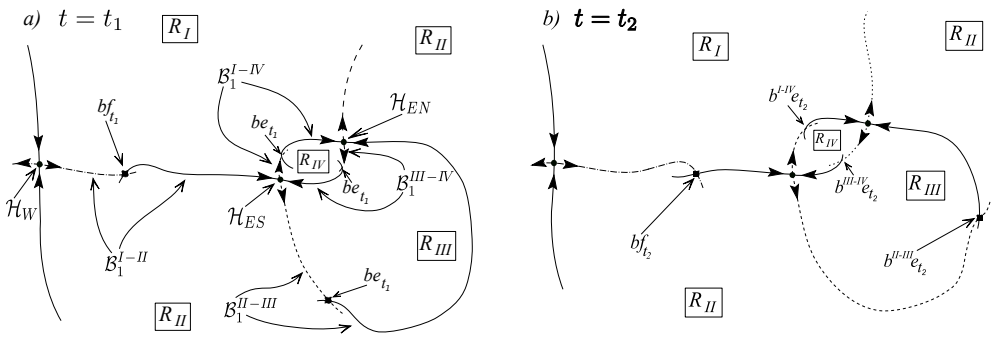

Figure 13: **Scenario II**. Construction of a time-dependent boundary, $\mathcal{B}^{I-III} \cup \mathcal{B}^{II-III} \cup \mathcal{B}^{I-IV} \cup \mathcal{B}^{III-IV}$, which separates distinct regions in the flow (R_I, R_{II}, R_{III} and R_{IV}) at two different 'observation' times (*a*) $t = t_1$ and (*b*) $t = t_2$. R_{III} denotes the large eddy region, which is also present in Scenario I, and R_{IV} marks the emergent small-eddy region. Compare this geometry with that of Scenario I shown in figure 6. Transport across this boundary can be analysed by considering turnstile lobes shown in figure 14.

to the small eddy region (see figure 13).

The boundary in this scenario is constructed in a similar way to that described for Scenario I in §4.1. We illustrate this process in figure 13. In addition to the front and the large eddy boundary intersection points, denoted by bf_{t_i} and $be_{t_i}^{II-III}$ respectively, we need to specify two additional *bips* on the boundary of the small eddy region R_{IV}, denoted by $be_{t_i}^{I-IV}$ and $be_{t_i}^{III-IV}$.

All of the transport routes discussed in the context of Scenario I are also present in Scenario II (see figure 18). In figure 14 we illustrate the construction of the appropriate simple turnstile lobes which mediate transport across different parts of the boundary.

There also exists new transport routes for this geometry which arise due to the presence of the two new boundary segments, $\mathcal{B}^{I-IV}$ and $\mathcal{B}^{III-IV}$. The simple turnstile lobe transport mechanism across these segments is illustrated in the insets of figure 14 (see the lobes marked by "✖✖", "✖", "▼▼" and "▼" in figure 14).

These transport routes can be observed in the flow field data obtained from the DieCAST model (§2) which we illustrate in figure 15. First, in figure 15a,b we show the entrainment of a lobe into the small eddy region, which proceeds according to the simple-lobe turnstile mechanism, from R_I into R_{IV} across the boundary segment $\mathcal{B}^{I-IV}$, as explained earlier for a simplified geometry in figures 13 and 14. The entrainment process is revealed in the geometry of the computed segments of stable and unstable manifolds associated with the hyperbolic trajectories $\mathcal{H}_{ES}$ and $\mathcal{H}_{EN}$ at two different times (days 683 and 687).

Next, in figure 15c,d we show the ejection of a simple lobe from the small eddy region into the large eddy region, which proceeds according to the same simple-lobe turnstile mechanism as before (cf. figure 14), although this time across the boundary segment $\mathcal{B}^{III-IV}$ in the direction $R_{IV} \rightarrow R_{III}$ (see the lobe marked by "▼" in figure 14).

Since the small eddy region exists in the studied flow for relatively short periods of time (i.e. it emerges and disappears several times in the available data set), we were able to detect at best a single lobe being entrained into the small eddy and a single lobe being ejected out of it. Another consequence of this very intermittent process is that

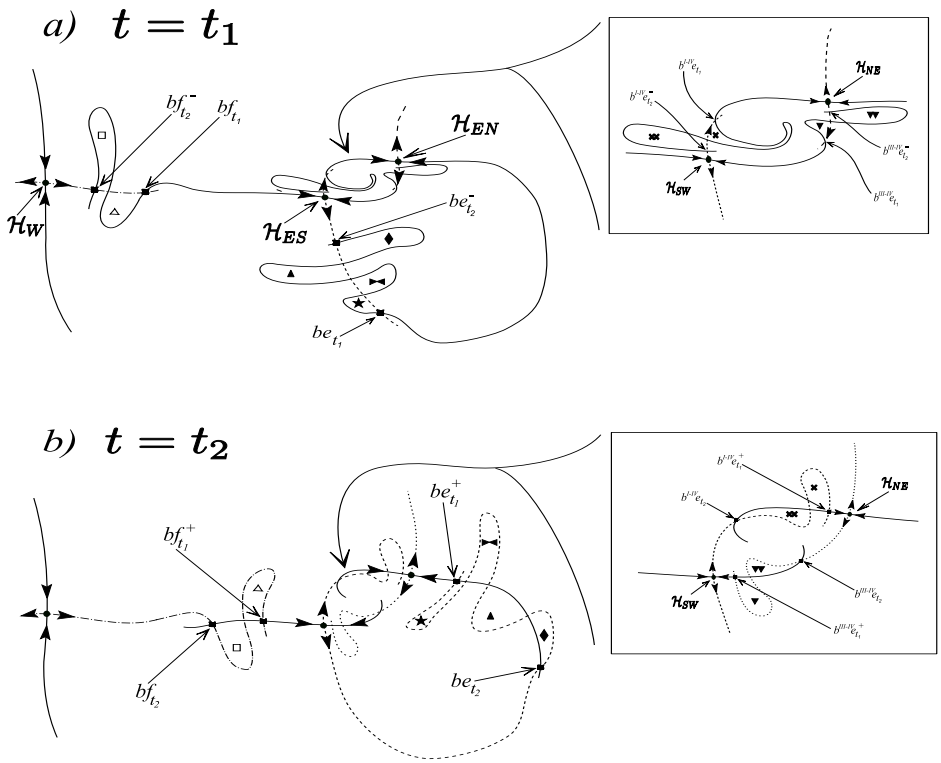

Figure 14: **Scenario II**. Schematic evolution of 'simple' turnstile lobes (i.e. lobes which do not overlap with other lobes) from $t = t_1$ to $t = t_2$. Transport across the front (see $\mathcal{B}^{I-II}$ in figure 13) and across the boundary segment $\mathcal{B}^{II-III}$ of the large eddy region is the same as in Scenario I. Transport across the boundary of the emergent small eddy region is illustrated in the insets.

we are only able to compute rather short segments of the invariant manifolds associated with the emerging small Lagrangian eddy which are only sufficient for visualising the simple-lobe turnstile mechanism in the data set.

In order to describe the transport mechanism responsible for diverting some of the warm water lobes which crossed the front (i.e. $R_{II} \to R_I$) back into the large eddy (i.e. $R_{II} \to R_I \to R_{IV} \to R_{III}$), we must understand how a fixed portion of fluid can be transported between these regions. The key to understanding this process lies in considering the evolution of the *composite lobes* associated with the small eddy boundary. Note that we encountered a similar situation earlier in §4.1 when discussing the long-term transport processes ($R_{II} \to R_{III} \to R_{II}$) due to the presence of the large eddy region. In figure 16 we illustrate the transport across the small eddy region for the simplest possible manifold geometry. We analyse this process by following the evolution of a portion of fluid (yellow patch in figure 16a) trapped inside a composite lobe which is identified by taking account of an additional structure inside the simple lobe marked by "✖✖" in figure 14. The additional complexity is due to a long segment of $W^s_{\mathcal{H}_{ES}}$ protruding, at $t = t_1$, into the lobe formed by the intersecting segments of $W^s_{\mathcal{H}_{EN}}$ and $W^u_{\mathcal{H}_{ES}}$. The evolution of the relevant lobes, leading to the eventual ejection of the marked fluid into R_{III}, is sketched at three subsequent time instants in figure 16b-c. In all insets we draw the same segments of $W^u_{\mathcal{H}_{ES}}(t_i)$ and $W^u_{\mathcal{H}_{EN}}(t_i)$ but, for visual clarity, we draw longer than the initial segments of $W^s_{\mathcal{H}_{ES}}$ (in the insets c,d)

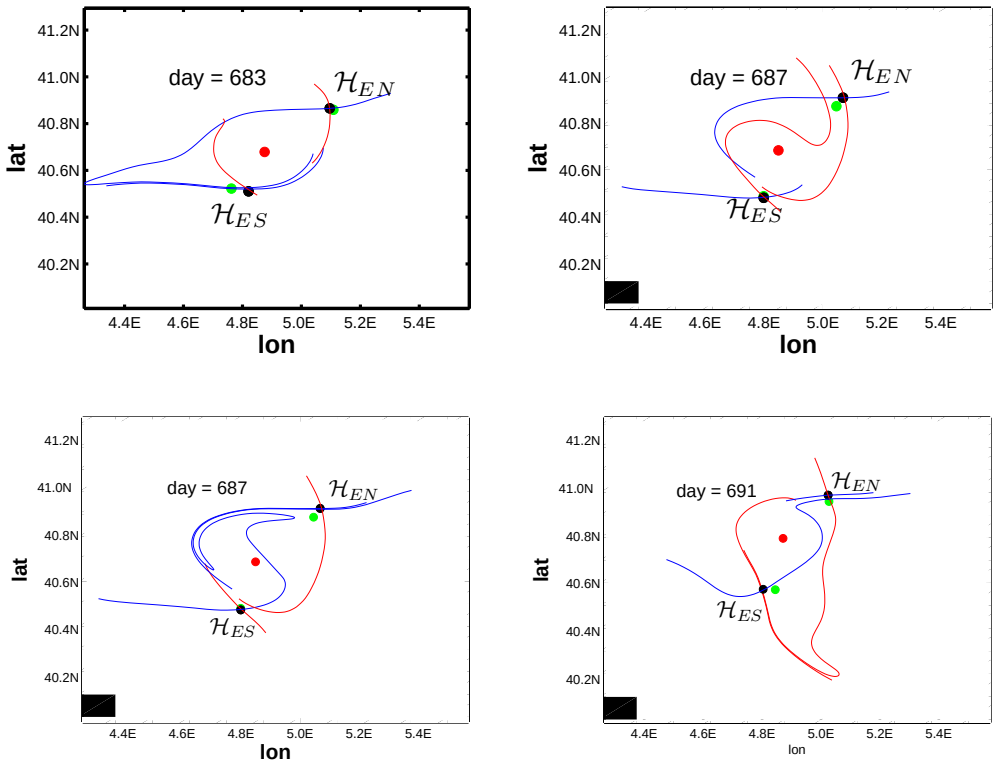

Figure 15: **DieCAST model, NW Mediterranean.** Entrainment of water from the region north of the front (R_I in figures 6, 13) into the small eddy region R_{IV} between days 683 (top left) and 687 (top right). The subsequent detrainment is shown in the two bottom insets (days 687 and 691). This process is characteristic of the Lagrangian geometry of Scenario II which emerges intermittently in the data set. The blue curves mark the stable manifolds of $\mathcal{H}_{EN}$ and $\mathcal{H}_{ES}$, the red curves mark their unstable manifolds, and the black squares denote the boundary intersection points.

and of $W^s_{\mathcal{H}_{EN}}$ (in d)) which result in a larger number of lobes than were present in the initial configuration shown in figure 16a.

Finally, in figure 17, we show an evidence obtained from the flow in the North-Western Mediterranean Sea for the existence of the Lagrangian mechanism, transporting some of the warm water filaments across the small eddy region into the large eddy region. Due to the relatively short period during which the small eddy region exists in the flow, we were unable to compute sufficiently long manifold segments of $\mathcal{H}_{ES}$ to determine the composite lobe structure illustrated in figure 16. The black curve shown in figure 17 shows the geometry of the computed unstable manifold of $\mathcal{H}_W$. The shaded region marks an overlap between a front lobe and a small eddy lobe. The front lobe containing the shaded area and formed by the intersecting segments of $W^u_{\mathcal{H}_W}$ and $W^s_{\mathcal{H}_{ES}}$, contains warm water transported earlier across the front from the South (i.e. $R_{II} \rightarrow R_I$ across $\mathcal{B}^{I-II}$), according to the previously described simple

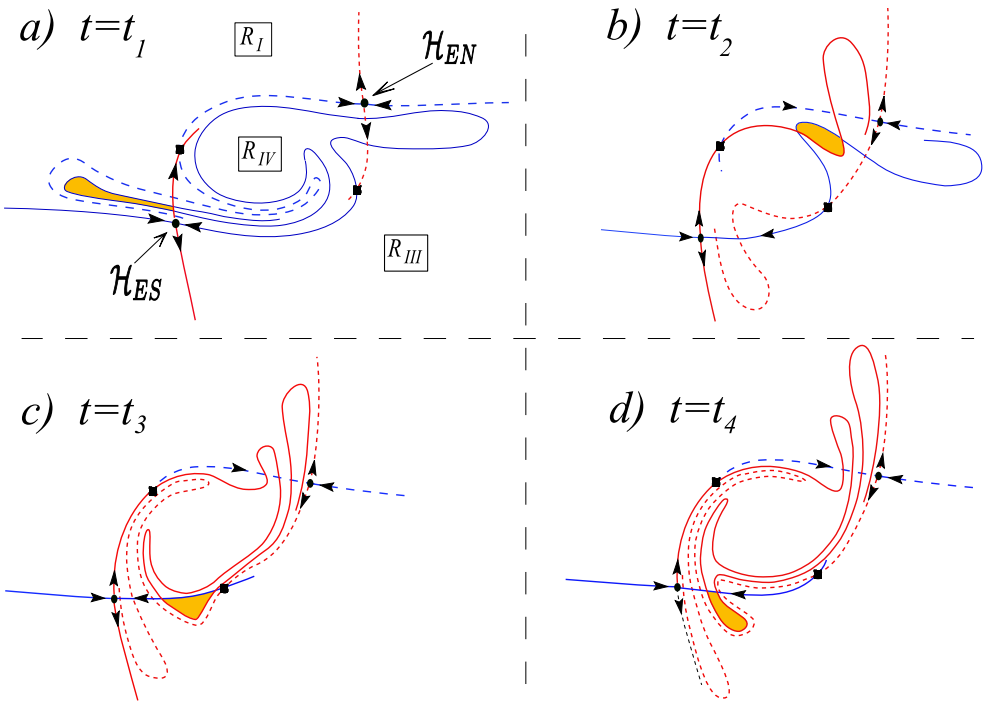

Figure 16: **Scenario II**. Entrainment of a front lobe into the large-eddy region R_{III} via the small-eddy region R_{IV} (only the neighbourhood of the small eddy is shown here). This mechanism, which is shown for the simplest possible manifold geometry, is responsible for entrainment of parts of front lobes from R_I to R_{III} and it cannot be accomplished in the absence of R_{IV} (see also figure 18).

lobe turnstile mechanism of cross-frontal transport. The overlapping area (shaded) between the front lobe and a small eddy lobe, is first entrained into the small eddy region (figure 17b) and subsequently ejected into the large eddy region (figure 17d). Note here that the existence of the overlapping area between the front and the small eddy lobe indicates an interaction between the front and the eddy pair. An example of a flow configuration flow in which such an interaction does not occur is discussed in §5.

In figure 18 we summarise the transport mechanisms discussed in the two previous sections in relation to Scenarios I and II by sketching transport routes of a tracer contained in northern lobes (blue; lobes that can be inverse mapped in time to the region R_I) and in southern lobes (green; lobes that can be inverse mapped in time to the region R_{II}). We assume here that the Lagrangian configurations of Scenario I or Scenario II exist in the flow for times long enough that all the indicated transport routes can be accomplished. If the Lagrangian flow structure evolves 'too rapidly' between the two configurations, or if it changes to a completely different structure, some of these routes may be terminated prematurely. Note finally that additional transport routes, not present in Scenarios I and II, might appear in the flow if the front-eddy system interacts significantly with other Lagrangian flow structures. For example, while following the evolution of a lobe associated with the large eddy (R_{III}), just like the one shaded in figure 11a, one could observe this lobe (or part of it) to travel South-West instead of moving counterclockwise around the perimeter of the large eddy. The

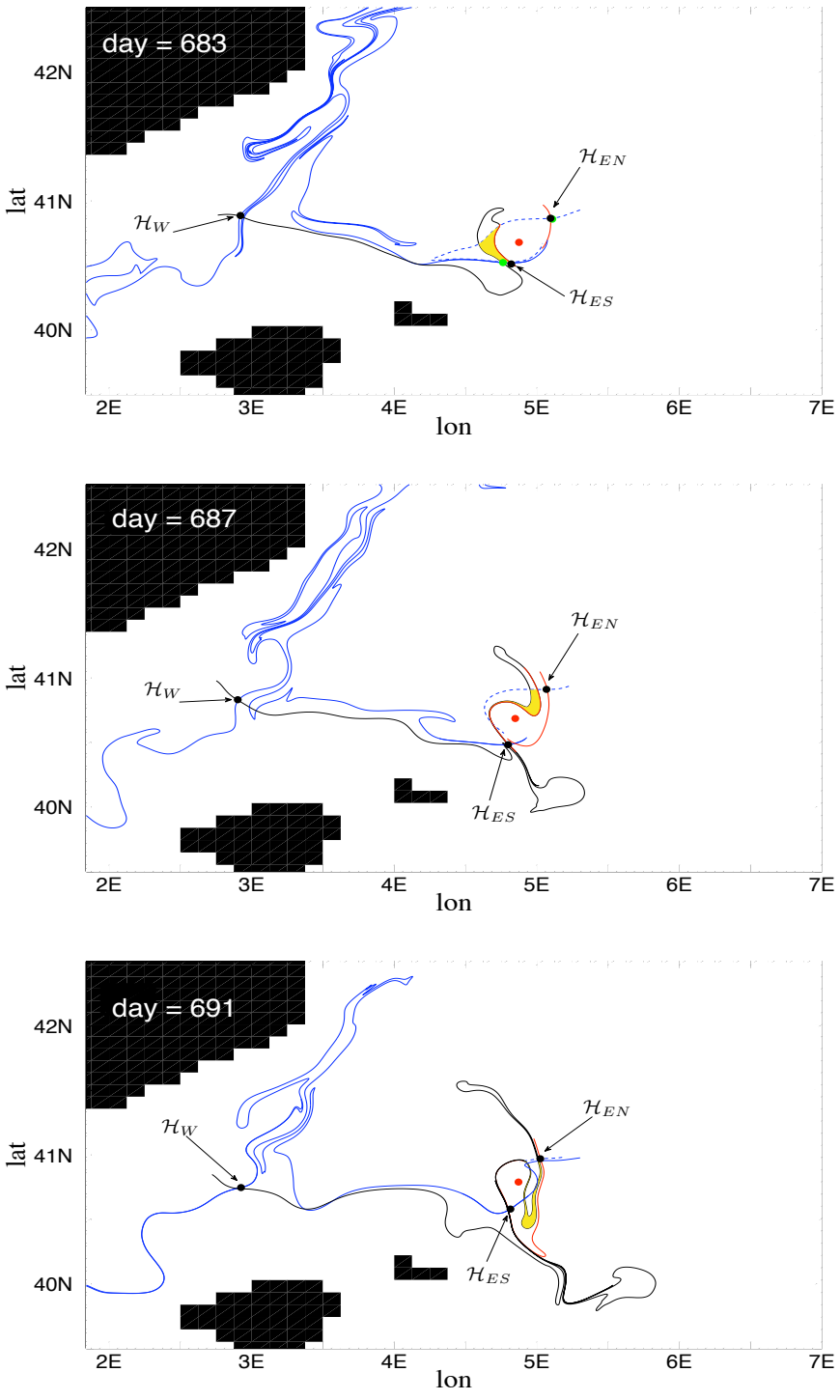

Figure 17: **DieCAST model, NW Mediterranean.** Interaction of a front lobe with a small eddy lobe, revealing a transport route ($R_{II} \to R_I \to R_{IV} \to R_{III}$; see also figure 18b) which is possible only when the flow evolves according to Scenario II for sufficiently long time. This route allows injection of a portion of hot southern waters which crossed the front inside a front lobe (shaded) into the large eddy region across the small eddy region R_{IV}, according to the mechanism sketched in figure 16.

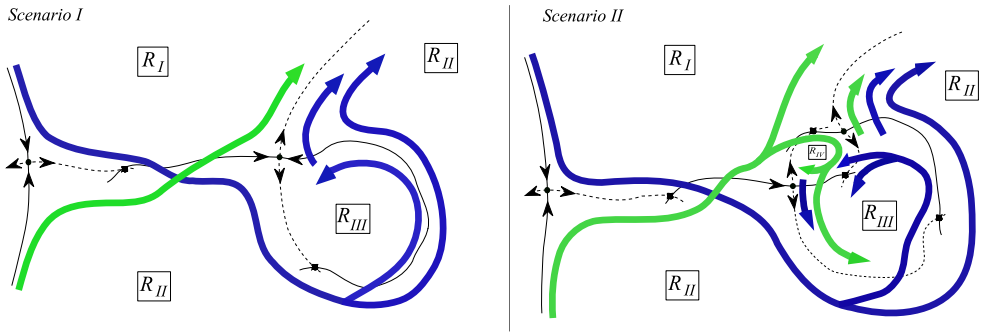

Figure 18: Possible transport routes for front lobes which originate near the stable manifold of $\mathcal{H}_W$ in the far North (blue) or in the far South (green) at $t \to -\infty$. Note that these transport routes may be terminated prematurely if the Lagrangian geometry of the underlying flow evolves into one different than those of Scenario I and II. Note also that the journey of the southern lobes indicated in Scenario II by the green branch: $R_{II} \to R_I \to R_{IV} \to R_{III}$ may be severely affected if the flow does not remain in the Lagrangian configuration of Scenario II for a sufficiently long time.

turnstile mechanism for transport associated with the invariant manifolds considered in Scenarios I and II does not allow for such a process to take place. A proper description of transport processes in such a case would therefore require considering the geometry of all intersecting invariant manifolds of an extended system, including the stable and unstable manifolds associated with the additional Lagrangian flow structure which interacts with the front-eddy system.

4.3 Time transition between Scenario I and Scenario II

As we mentioned several times in the previous sections, the studied example of the flow in the North-Western Mediterranean Sea shows an intermittent evolution between the flow structures of Scenario I and II. The transition between the two flow structures is usually highlighted by an (Eulerian) bifurcation of the ISPs in the flow, leading to the appearance or disappearance of the second smaller eddy. We managed to understand the Lagrangian transport mechanisms associated with each of these scenarios by uncovering the structure of intersecting stable and unstable manifolds of the relevant DHTs in the flow within conveniently chosen time intervals. Recall that we identified two such DHTs ($\mathcal{H}_W$ and $\mathcal{H}_E$), together with their stable and unstable manifolds, in order to describe the geometry of the front interacting with the Lagrangian eddy in Scenario I (see figures 5a and6). In the Lagrangian description of Scenario II we considered three DHTs ($\mathcal{H}_W$, $\mathcal{H}_{SW}$ and $\mathcal{H}_{NE}$) and their invariant manifolds in order to define the front interacting with two Lagrangian eddies (see figure 5b and 13). Clearly, in order to understand how the manifold tangle associated with the two DHTs of Scenario I can evolve into the manifold tangle of three DHTs in Scenario II, we first need to understand the relationship between the two sets of DHTs throughout the time interval corresponding to the transition. Then, we can understand the effect of such a transition on the Lagrangian transport in the underlying flow by analysing the evolution of the relevant invariant manifolds. Lagrangian descriptions of flow transitions of this type have received little attention in the geophysical fluid dynamics literature and there is no rigorous mathematical theory to guide our analysis.

In order to isolate the relevant geometrical structures and behaviour in a controlled

setting we first consider a kinematic model of the local flow in the front-eddy system in the neighbourhood of the bifurcating ISPs, given by the streamfunction

$$\psi = -s(t)xy + (v(t)/2\delta)e^{-\delta(x^2+y^2)} + \beta(y-x), \qquad s, v, \delta, \beta \geqslant 0 \tag{9}$$

where the first term represents the linear, time-dependent strain, the second term represents a time-dependent vortex flow, and the last term represents a uniform flow. The choice of the amplitude functions $s(t)$ and $v(t)$ will determine a particular scenario; it will soon become clear that the amplitude of the uniform flow β represents a symmetry breaking parameter when considering bifurcations of the ISPs present in the flow.

The velocity field corresponding to (9) is given by:

$$\left.\begin{aligned} \dot{x} &= -s(t)x - v(t)e^{-\delta(x^2+y^2)}y + \beta \\ \dot{y} &= s(t)y + v(t)e^{-\delta(x^2+y^2)}x + \beta \end{aligned}\right\} \tag{10}$$

It is straightforward to determine that the ISPs in such a flow must lie on the line $y = -x$ and that, assuming $x, y \ll 1$, their location on this line in terms of distance from the origin, $\varrho = (x^2 + y(x)^2)^{1/2}$, is given by the roots of

$$F(\varrho) = (v - s)\varrho - v\varrho^3 + \beta + \mathcal{O}(\varrho^5). \tag{11}$$

The first two terms in (11) can be recognised as the normal form of a pitchfork bifurcation. We note that in our setting the bifurcation parameter, $\lambda = v(t) - s(t)$, is actually a function of time; β is in this case one of the unfolding parameters of this normal form into a corresponding non-degenerate, third-order form $\tilde{F} = (v - s)\varrho + v\varrho^3 + \alpha\varrho^2 + \beta$. Provided the bifurcation parameter λ increases monotonically in time ($\dot{\lambda} > 0$) there is one hyperbolic ISP in the system before the bifurcation takes place at, say t_{bif}, and there are three ISPs (one elliptic and two hyperbolic) after the bifurcation.

In figure 19 we illustrate two different possible bifurcations of the ISPs which can be obtained in system (10) from the unfolding of (11) for different values of β. The sketches shown in figures 19a,b correspond to an asymptotically steady evolution of (10) when $\lambda(t)$ has the form of a sigmoid (figure 19c). The sketches shown in figures 19c,d illustrate the same two types of bifurcations as in figures 19a,b but with λ varying in time in a more complicated fashion. In the symmetric case, when $\beta = 0$ (codimension-two bifurcation), the original ISP bifurcates into three new ISPs in a familiar pitchfork bifurcation (figure 19a,d), which occurs at t_{bif} such that $v(t_{\text{bif}}) = s(t_{\text{bif}})$. When $\beta \neq 0$, two new ISPs, one elliptic and and one hyperbolic, are born in a saddle-nodle bifurcation and exist, for $t > t_{\text{bif}}$, alongside the original ISP (figure 19b,e).

Consider now the system (10) on the time-interval, $\mathcal{T} = [t_i,\ t_f]$, containing the bifurcation time of the ISPs (i.e. $t_{\text{bif}} \in \mathcal{T}$) so that the flow evolution corresponds locally to the transition between Scenarios I and II. We study first an asymptotically steady evolution of (10) by setting set $s = 1$ and $v = \text{atan}(5\,t) - \text{atan}(5\,t_i)$ (cf. figure 19c). This represents a flow evolving from a pure strain, characterised by a single hyperbolic ISP, to the familiar cat's-eye flow, having two hyperbolic ISPs. The advantage of considering such a time dependence lies in the fact that, if we allow $\mathcal{T} = \mathbb{R}$, the DHTs present in the flow must necessarily converge to the hyperbolic ISPs of (10) for $t \to \pm\infty$, since these ISPs are the only bounded, hyperbolic trajectories in the steady flow limit.

If there is a symmetric pitchfork bifurcation in the flow (10) (i.e. when $\beta = 0$), the two continuous paths of hyperbolic ISPs which exist throughout the time interval $\mathcal{T}$ can be used as the initial guesses in the DHT-finding algorithm [22]. Results of

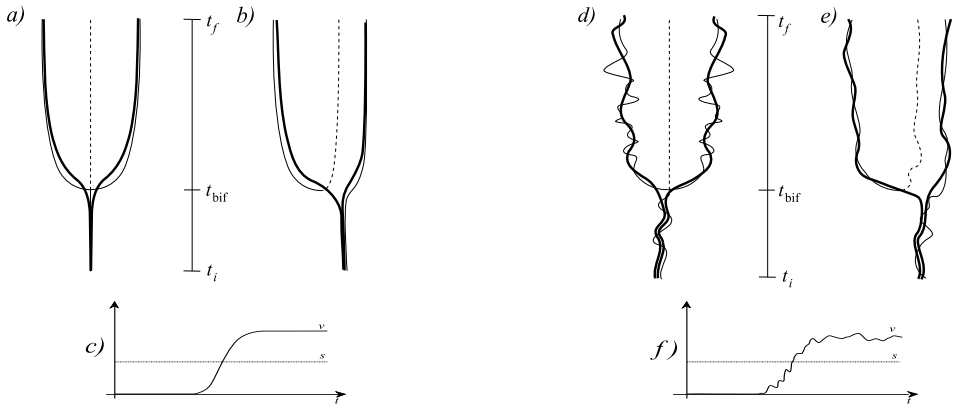

Figure 19: Sketches of projections of the ISP's (thin) and the DHT's (thick) onto the plane $(x, y, t) = (x, -x, t)$ in the extended phase space of the system (10), corresponding to two unfoldings of the normal form for the pitchfork bifurcation (11). a,b,c) the asymptotically steady evolution of (10) and d,e,f) an arbitrary time depedence.

this procedure are presented in figure 20a where the computed DHTs are shown as black curves in the extended phase space of the system (spanned by the two spatial directions and time). The green surface also shown there is obtained by recording the time-evolution of the unstable manifolds of the two DHTs in the extended phase space. These two (finite-length) manifold segments are so close tho each other that they are virtually indistinguishable numerically. Note that as the DHTs diverge from each other, parts of their unstable manifolds are rolled up around the (red-coloured) trajectory which coincides with the bifurcated elliptic ISP, indicating the the centre of an eulerian eddy. In order to identify the boundary of the Lagrangian eddy, defined earlier in §3.1, we would also have to show the geometry of the stable manifolds of the two DHTs, which we avoid for visual clarity. The computed DHTs approach each other for $t < t_{\rm bif}$, when following them backward in time (see also figure 22), and they become virtually indistinguishable when $t \to -\infty$ (not shown). It can also be seen that for $t \to t_i$ or $t \to t_f$, when the system (10) is effectively time-independent due to our choice of the amplitudes, $v(t)$ and $s(t)$, the two DHTs converge towards the paths of ISPs, as expected.

When the system (10) undergoes the saddle-node bifurcation of the ISPs (i.e. when $\beta \neq 0$), the problem of computing the DHTs in the flow becomes more cumbersome. In such a case we only have one path of ISPs which stretches across the whole time interval $\mathcal{T}$. Consequently, we have only one 'good' guess which allows us to find, using the iterative DHT-finding algorithm, the location of only one of the two the DHTs which we expect to be present in the flow, at least in the asymptotically steady case. However, based on the geometry described for the symmetric case and the fact that for $\beta \ll 1$ the saddle-node bifurcation of the ISPs takes place close to the original path of ISPs (see (11)), we can attempt to construct a continuously differentiable (hyperbolic) guess for the second DHT by extending the bifurcated hyperbolic path of ISPs backward in time in such a way that it approaches the first DHT (in a time-backward sense) when $t_{\rm bif} - t \gg 1$. This heuristic method proves very useful in locating the second DHT for the class of problems we consider (we do not, as yet, have more rigorous estimates on the range of situations for which such a method is successful).

In figure 20b we show the results of computations performed in the system (10)

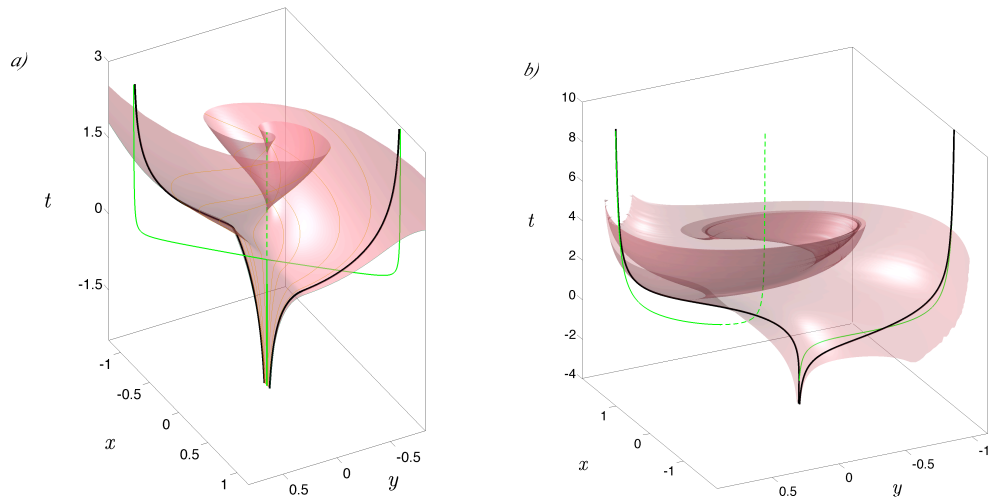

Figure 20: Geometry of the DHTs (black) and their unstable manifolds (red) computed for the system (10) in the asymptocially steady case when: a) the symmetric pitchfork bifurcation ($\beta = 0$) of the system's ISPs (green) takes place; b) the saddle-node bifurcation of the system's ISPs occurs ($\beta \neq 0$).

having the same time dependence as that used in figure 20a but undergoing the saddle node bifurcation of the ISPs (i.e. $\beta \neq 0$). The DHTs identified in the flow are shown as the thick black curves. The paths of the hyperbolic ISP are shown in green and the path of the elliptic ISP is shown in red. It is again remarkable that the computed segments of unstable manifolds of the two DHTs seem to coincide throughout the whole time interval $\mathcal{T}$. The surface corresponding to the time evolution of the unstable manifold of one of the DHTs is shown in olive-green and the surface for the other DHTs is numerically indistinguishable from the one shown. The asymptotic steady streamline pattern is again the 'cat's eye' pattern even though the Eulerian characteristics of the transition to this configuration, i.e. the bifurcation of the ISPs, was rather different.

Finally, we apply the procedure for identifying the DHTs and their manifolds during the transition between Scenario I and II in a flow that is not asymptotically steady. We illustrate this process using a more complex and realistic flow obtained from the kinematic model of the whole front-eddy system, discussed in more detail in §5. In figure 21 we show the geometry of the the two DHTs associated with the small eddy region, $\mathcal{H}_{ES}$ and $\mathcal{H}_{EN}$, when the examined flow undergoes a transition from the geometry of Scenario I to that of Scenario II, accompanied by a saddle-node bifurcation of ISPs. When following the evolution backward in time, one can see how the two DHTs approach each other and become virtually indistinguishable. Moreover, the computed segments of the unstable manifolds of the two DHTs are virtually indistinguishable throughout the time interval considered, even after the transition. The geometry of the stable manifolds, $W^s_{\mathcal{H}_{ES}}$ and $W^s_{\mathcal{H}_{EN}}$, of the two DHTs evolves in a more complex fashion during the transition and we show an example of this process in figure 22. Three important conclusions can be drawn from this example:

1) It can be clearly seen there that the two computed, finite-length segments of the stable manifolds are very close to each other at all times in the region corresponding to the large eddy away from the small eddy (cf. figures 6, 13). This implies that, even though the boundary of the large eddy could be considered as having a fine structure,

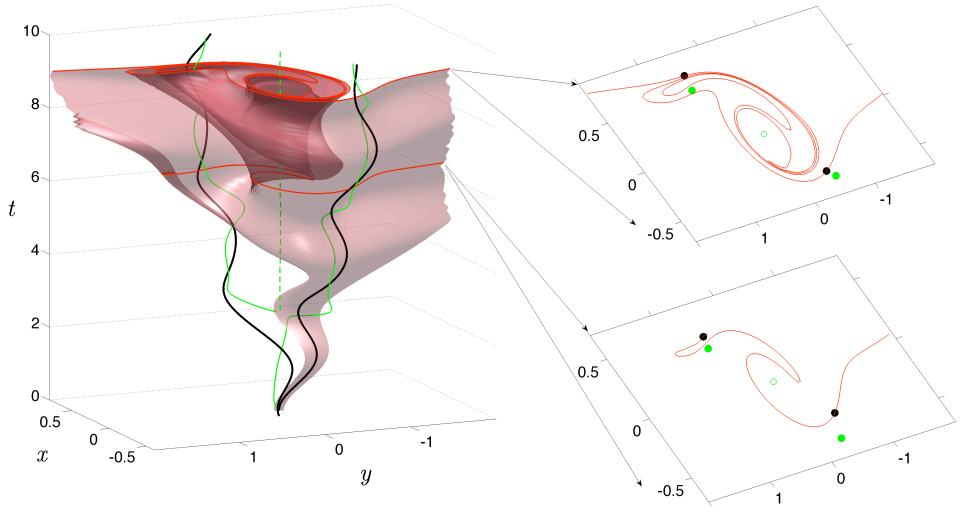

Figure 21: Geometry of the DHTs (black) and local geometry of their unstable manifolds (red) computed for the kinematic model discussed in §5 in the neighbourhood of the bifurcation ISPs (green). In this case, the two new ISP are born in the saddle-node bifurcation.

associated with the tightly packed segments of the two stable manifolds, $W^u_{\mathcal{H}_{ES}}$ and $W^u_{\mathcal{H}_{EN}}$, any lobes that could be formed by the intersections of this structure with the unstable manifolds would have a negligible area and would not therefore affect the Lagrangian transport across the corresponding boundary.

2) The manifold structure associated with Scenario I can be regarded as being made up of two almost identical copies of manifolds: one associated with $\mathcal{H}_{ES}$ and the other associated with $\mathcal{H}_{EN}$. Since these two structures, including the DHTs, are practically indistinguishable during the operation of Scenario I, we can identify the DHT labelled $\mathcal{H}_E$ in the description of Scenario I with any of the two DHTs, $\mathcal{H}_{ES}$ or $\mathcal{H}_{EN}$, associated with the small eddy in Scenario II.

3) During the transition from Scenario I to Scenario II, the two stable manifolds separate only in the neighbourhood of the two DHTs with which they are associated. This allows one to identify the boundary of the small Lagrangian eddy formed by segments of the unstable manifolds intersecting independently $W^s_{\mathcal{H}_{ES}}$ and $W^s_{\mathcal{H}_{EN}}$. Thus, although both these DHTs exist within the time interval when the flow evolves according to Scenario I, we only need to consider one DHT (labeled $\mathcal{H}_E$ in Scenario I). In figure 22, we show the geometry of the stable manifolds regardless of whether the flow evolves according to Scenario I or II.

To summarise, from the analysis of the kinematic model we have learned the following which appear to be the essential geometrical and kinematical features of the flow that are involved in the structural transition of the flow from Scenario I to Scenario II that is associated with the birth of a satellite eddy near the Eastern DHT ($\mathcal{H}_E$) recognised in Scenario I (§4.1). The emergence of the satellite eddy requires the presence of an additional DHT in the flow which remains very close the $\mathcal{H}_E$ during the time interval associated with flow evolution described by Scenario I. (The additional DHT is denoted as $\mathcal{H}_{NE}$ in the description of Scenario II, discussed in §4.2, and $\mathcal{H}_E$ from Scenario I is equivalent to $\mathcal{H}_{SW}$ in Scenario II.) Moreover, the stable and unstable manifolds of these two DHTs, or at least the finite-length segments of the computed

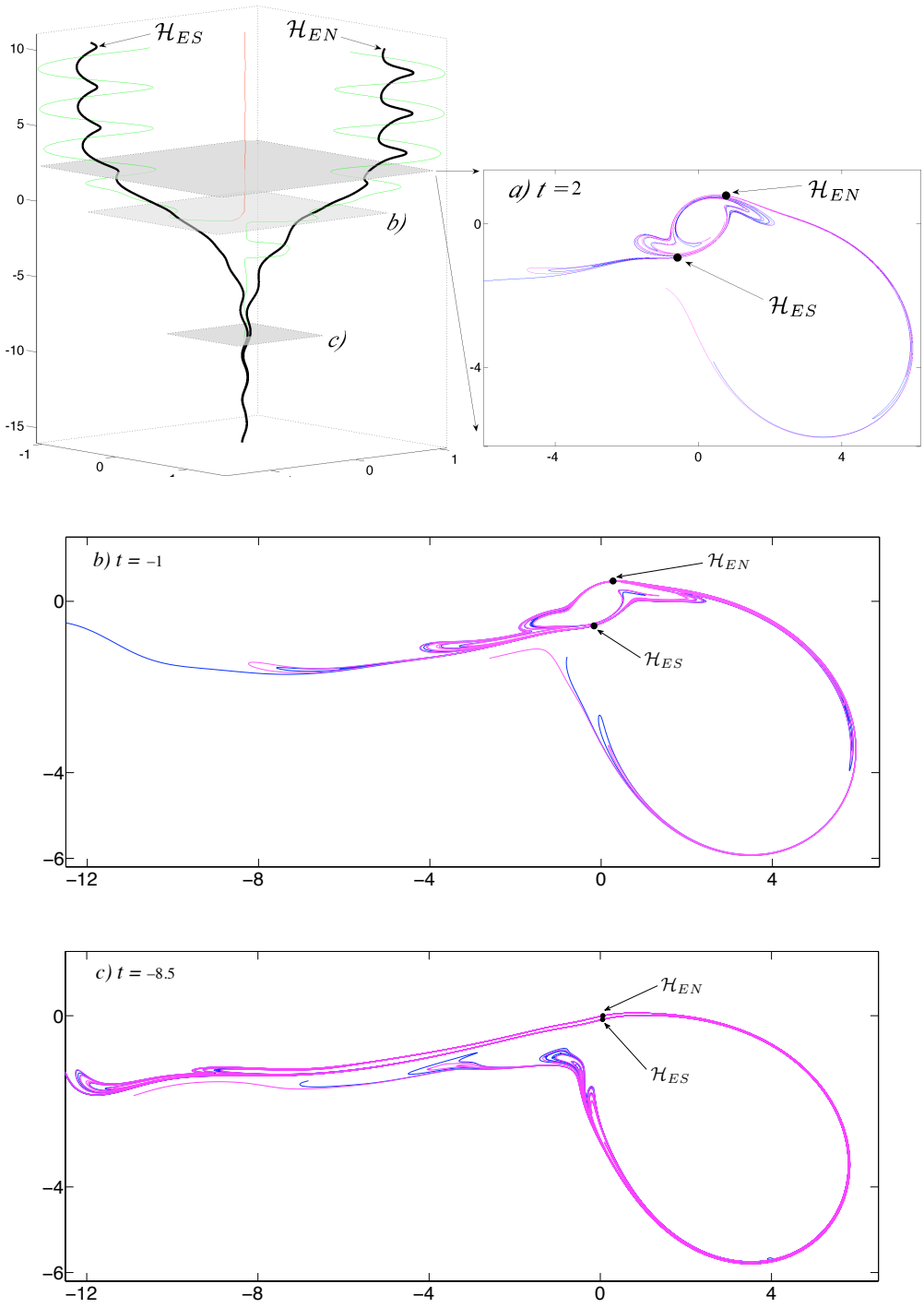

Figure 22: Evolving geometry of the stable manifolds of the two DHTs, $\mathcal{H}_{ES}$ and $\mathcal{H}_{EN}$, during the transition between Scenarios I and II which leads to the appearance of the small Lagrangian eddy. The two DHTs and their manifolds shadow each other during the evolution characteristic of Scenario I (c) which, from the point of view of transport, allows one to consider a single DHT, $\mathcal{H}_E$, and its manifold structure in Scenario I (see figures 6, 7). Note that during the transition this structure unfolds only in the neighbourhood associated with the small eddy.

manifolds, also remain very close to each other before the transition. During the birth of the second eddy, the DHTs diverge from each other along the unstable manifold of $\mathcal{H}_E$ so that their unstable manifolds remain 'shadowing' each other even after the transition (figures 20, 21). The stable manifolds of the two DHTs, denoted as $\mathcal{H}_{SW}$ and $\mathcal{H}_{NE}$ according to the nomenclature of Scenario II, do not coincide after the transition and their transverse intersections with the unstable manifolds can be used to determine the boundary of the second eddy (figures 13, 14). The precise verification of this scenario for transition between Scenario I and Scenario II in the data generated by the DieCAST model is not attempted here since, due to relatively short periods of operation of Scenario II in the flow, we could not compute sufficiently long stable and unstable manifolds associated with the two DHTs.

5 A kinematic Model

For different regions and times in our data set it is possible to consider much more complex interactions of flow structures that those considered in this paper. Indeed, the same can be said to be true for different regions and times in the ocean. Kinematic models have proven to be ideal "laboratories" for understanding the influence of flow structures on transport. We derive here a kinematic model of an 'extended' front-eddy system, i.e. a flow composed of a westerly current and an arbitrary number of Eulerian eddies, which we use to address further issues regarding the interaction (or lack of it) between neighbouring, localised flow features. Despite not being dynamically consistent, this model has the advantage of allowing us to study various aspects of transport processes in front-eddy systems in a controlled manner, which is an impossible task for a given set of experimental data and a formidable procedure in the case of high resolution numerical simulations. We focus here only on a few aspects of such kinematic flows which seem the most relevant to the transport mechanisms discussed in the context of the Lagrangian flow configurations of Scenario I and II. Undoubtedly, a more thorough analysis and a validation of such a model is needed. This is, however, beyond the scope of the present discussion.

Consider a time-dependent, two-dimensional, incompressible flow given by the following streamfunction:

$$\begin{aligned}\psi = &\Big(\mathcal{L}(t) - \alpha(t)\big(x\cos\theta(t) - y\sin\theta(t)\big)^2 + \beta(t)\big(x\sin\theta(t) + y\cos\theta(t)\big) \\ &+ \sum_{i=1}^{N} \mathcal{A}_i(t) e^{-\left((x-x_i(t))^2+(y-y_i(t))^2\right)/\delta_i(t)^2} \Big) \, \operatorname{atan}\big[\mu(t)(x+\sigma(t)\big], \end{aligned} \tag{12}$$

where $\mathcal{L}$, α, β, θ, $\mathcal{A}_i$, x_i, y_i, δ_i denote some arbitrary functions of time; $\mathcal{L}(t)$, $\alpha(t)$ and $\beta(t)$ control a flow component with parabolic instantaneous streamlines whose axis of symmetry at time t is inclined at the angle $\theta(t)$ to the y-axis. The remaining terms represent a collection of Eulerian vortices centered at $(x_i(t), y_i(t))$ and characterised by $\mathcal{A}_i(t)$ and $\delta_i(t)$. The sigmoidal envelope, given by the last multiplicative term in (12) and characterised by $\mu(t)$ and $\sigma(t)$ assures the existence of a westerly current in the flow.

The wealth of the time-dependent parameters present in the model allows one to study a large number of flow configurations which might be useful in more detailed studies of transport in vortex-dominated oceanic flows. In what follows we set

$$\alpha = 0.08,\ \beta = 1,\ \theta = -\pi/4,\ \mu = 0.2,\ \sigma = 17, \tag{13}$$

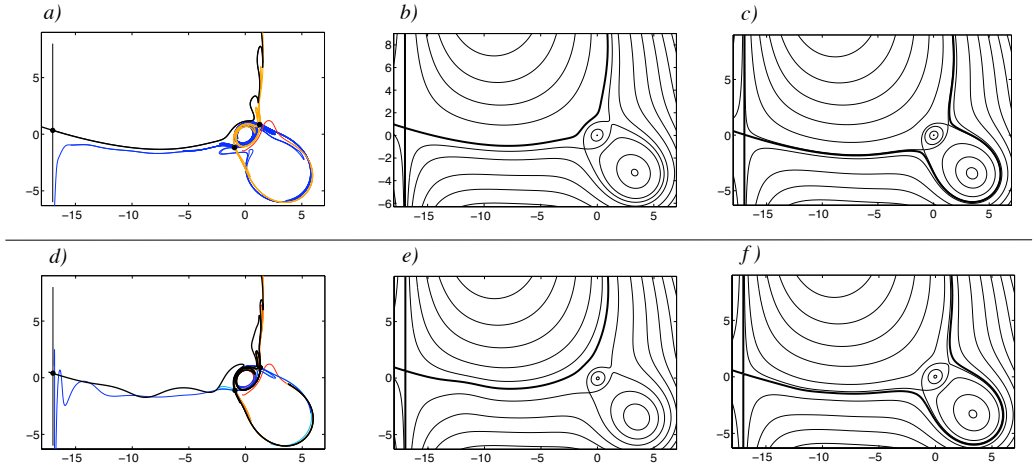

Figure 23: Comparison between the Lagrangian (a,d) and the Eulerian (b,c,e,f) viewpoints based on the kinematic model (12). Computations were performed for two different sets of parameters of the model: (a,b,c) show Run 1 characterised by (14) and (16); (d,e,f) show Run 2 characterised by (14) and (17). For both runs the Eulerian snapshots (b,c,e,f), showing an 'antipodal' geometry of the instantaneous separatrices of $\mathcal{H}_W$ (thick) which is revisited quasiperiodically, are qualitatively the same. In Run 1, the unstable manifold of $\mathcal{H}_W$ does not intersect the stable manifolds of $\mathcal{H}_{ES}$ and $\mathcal{H}_{EN}$, which results in a lack of cross-frontal transport (see also figure 14).

and we restrict our attention to two examples of quasiperiodically time-dependent flows which we seem to be particularly useful in illustrating the discrepancies between the Lagrangian and the Eulerian viewpoints when studying transport of a passive scalar in time-dependent flows.

Consider first a flow which, in the Eulerian framework, consists solely of a strong westerly current and a neighbouring eddy pair. Such a flow can be realised in the kinematic model (12) by setting, for example,

$$\mathcal{A}_1 = 10, \quad (x_1, y_1) = (4, -4), \quad \delta_1 = 4 + 0.4\sin(2.13t), \tag{14}$$

$$\mathcal{A}_2 = -2, \quad (x_2, y_2) = (0, 0), \quad \delta_2 = 0.9 + 0.2\sin(2.33t). \tag{15}$$

Then, the $i = 1$ vortex corresponds to the large eddy considered in Scenarios I and II and the $i = 2$ vortex corresponds to the small eddy present only in Scenario II. We then consider two slightly different configurations which, from the Eulerian viewpoint, undergo a very similar evolution.

First, we set

$$\mathcal{L}(t) = -1.25 + .75\cos(3t), \tag{16}$$

in addition to (13) and (14), and refer hereafter to the resulting flow as 'Run 1'. Figure 23a shows a snapshot of the relevant invariant manifolds in this flow and the insets b,c) present two snapshots of the instantaneous streamline patterns, showing 'antipodal' configurations between which the flow oscillates in a quasiperiodic manner. In figure 23b the unstable separatix line (thick) of the westernmost instantaneous

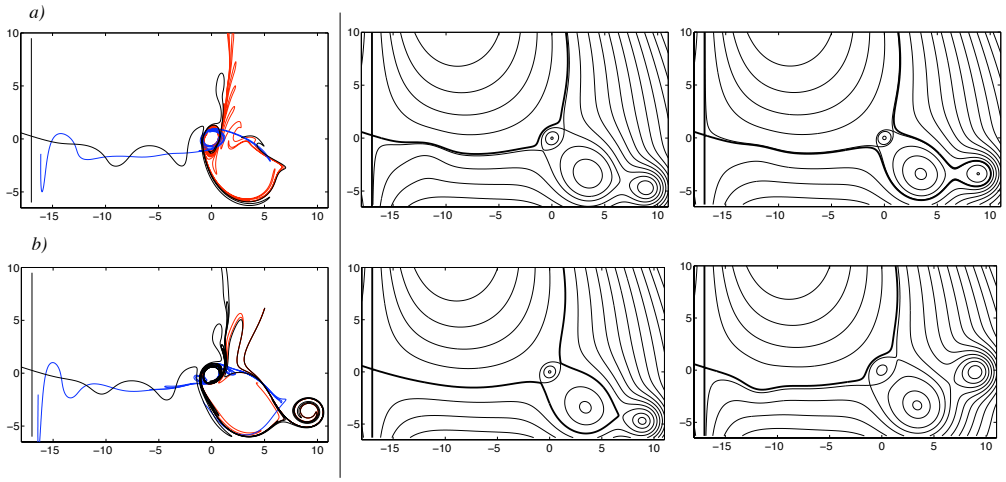

Figure 24: Effect of the presence of an additional Eulerian eddy, oscillating latitudinally to the East of the front-eddy system, on the Lagrangian geometry of Scenario II (see figures 13-16). Computations performed using the kinematic model (12) for two different frequencies of the latitidinal oscillations of the additional eddy given by (22) in a) and by (23) in b) . The sequence of topologically distinct instantaneous streamline patterns (right) can be observed in both runs, although their relative duration and order in which they appear is different. In a) the Lagrangian geometry of the flow is equivalent to that of Scenario II (i.e. no interaction with the additional eddy) while in b) it is not (i.e. additional interactions present).

stagnation point is located North of the eddy-pair system and in c) it encompasses the two eddies from the South.

A similar Eulerian evolution of the velocity field takes place when, in addition to (13) and (14), we set

$$\mathcal{L} = -1.25 + .8\cos(t),\ \mathcal{A}_3 = -0.8\cos(1.57t - 0.3),\ (x_3, y_3) = (-12, -2),\ \delta_3 = 2. \quad (17)$$

We refer hereafter to this flow as 'Run 2'. As it can be seen in the insets e,f) of figure 23, the Eulerian snapshots of the 'antipodal' instantaneous streamline patterns in Run 2 are very similar to those recorded in Run 1 (insets b,c), although they occur at different times during the evolution. However, the Lagragian geometry, revealed in the structure of the relevant invariant manifolds in both these flows, differs significantly between the two cases. In Run 1 (figure 23a) the unstable manifold of $\mathcal{H}_W$ does not intersect any of the stable manifolds of the DHTs associated with the eddy pair (see $\mathcal{H}_{ES}$ and $\mathcal{H}_{EN}$ in figure 14), which results in a lack of cross-frontal transport. in Run 2 the unstable manifold of $\mathcal{H}_W$ inersects with the stable manifold of $\mathcal{H}_{ES}$ (see figure 23d) and the cross-frontal transport proceeds as in §4.2.

We now turn our attention to a problem we mentioned only briefly until now which, similarly to the previous example, concerns the interaction between neighbouring, localised flow structures. When describing transport mechanisms in flows characterised by an interplay between the Lagrangian configurations of Scenario I and II (§4.1, §4.2), we implicitly assumed that other, localised flow features did not affect the transport routes in our isolated front-eddy system at least during the time interval considered. In realistic flows, as can be seen for example in figures 1, 2, there are many other Eulerian vortices in the neighbourhood of the front-eddy system, and it is often very

difficult to asses from the Eulerian flow evolution whether or not such a system can be indeed regarded as isolated within any finite-time interval. We provide some insight into this problem using again the kinematic model (12), although we stress that these conclusions should be treated with caution when analysing physical, or at least dynamically consistent, flows.

Consider a flow obtained by substituting the constants (13), $\mathcal{L} = -1$ into (12) and choosing

$$\mathcal{A}_1 = 10, \qquad (x_1, y_1) = (4, -4), \qquad \delta_1 = 4 + 0.1\sin(2.13t), \tag{18}$$

$$\mathcal{A}_2 = -2, \qquad (x_2, y_2) = (0, 0), \qquad \delta_2 = 0.9 + 0.5\sin(2.33t), \tag{19}$$

$$\mathcal{A}_3 = -2\cos(1.57t - 0.3), \quad (x_3, y_3) = (-12, -2), \quad \delta_3 = 2, \tag{20}$$

$$\mathcal{A}_4 = 13, \qquad \delta_4 = 2 + 0.1\sin(1.7t)^2. \tag{21}$$

Such a flow contains, in addition to the westerly current and the eddy pair at its eastern end, two additional Eulerian vortices. The i=3 vortex, which was also present in Run 2 shown in figure 23, is not revealed in the instantaneous streamline patterns but it strengthens the interaction between the front and the eddy pair. The i=4 Eulerian vortex oscillates latitudinally on the eastern side of the front-eddy system. Figure 24a reveals a snapshot of the invariant manifolds of the front-eddy system when the location of this vortex changes according to (Run 3)

$$(x_4, y_4) = \big(\, 9.3, -2.3 + 2.5\sin(5t) \,\big), \tag{22}$$

and figure 24b shows the front-eddy manifolds when the i=4 vortex oscillates less rapidly, according to (Run 4)

$$(x_4, y_4) = \big(\, 9.3, -2.3 + 2.5\sin(t) \,\big). \tag{23}$$

The remaining insets in figure 24 show a collection of topologically distinct snapshots of the instantaneous streamline patterns which are present in both flows, although they evolve into one another in a different order and at different times in the two cases. Clearly, the manifold configuration in Run 3 is topologically equivalent to that discussed in the context of transport in Scenario II. Consequently, the front eddy system can be regarded as isolated. In Run 4 (figure 24b), however, the slower oscillations of the i=4 vortex affect the Lagrangian geometry of the system and induce an interaction of the vortex with the remaining structure. The parameters used in this example were deliberately chosen in such a way that the resulting flows had different underlying Lagrangian geometry, despite the Eulerian evolution being qualitatively very similar. It might be of interest that we were not able to observe the interaction of the i=4 eddy with the front-eddy system when it was located sufficiently far away from it, so that at no time instant there existed an instantaneous streamline encompassing the large eddy (i=1) and the i=4 eddy.

Studies of the kinematic model suggest a variety of additional questions whose answers may play an important role in understanding Lagrangian transport in complicated data sets with a variety of (possibly transient) flow structures. A few such questions coming from the above simulations are the following:

- Is the size of the second eddy important in enhancing the mixing in the main gyre?

- What is the most important (kinematically) ingredient in the variability of the eddy system (i.e. variations in the spatial extend of the second eddy, variations in the position of its centre, etc.) for the enhanced mixing in the main gyre?
- (Related to the first question) The emergence of an additional small Lagrangian eddy associated with the transition between Scenarios I and II can be, in principle, nested infinitely many times by inducing subsequent pitchfork or saddle-node bifurcations of each bifurcated hyperbolic ISP. Is such a 'subgrid' structure important in regard to the efficiency of stirring in the dominant gyre?
- The transition between the two flow configurations, given by Scenarios I and II, is usually highlighted by an (Eulerian) bifurcation of the ISPs in the flow, leading to the appearance or disappearance of the second smaller Eulerian eddy in the velocity data. If the lifetime of the new Eulerian is long enough, the Lagrangian structure 'catches up' by transiting from Scenario I to Scenario II. What is the critical lifetime of the small eddy below which the relevant DHTs do not significantly react to this Eulerian event and the Lagrangian transition between Scenarios I and II does not take place?

Finding the answers to these questions is left to future work, but the answers will undoubtedly lead to further both a further development of the dynamical systems approach to Lagrangian transport as well as a deeper insight into Lagrangian transport in complex data sets.

6 Conclusions

In this paper we have continued the study started in [28] of Lagrangian transport in the Northwestern Mediterranean Sea, near the North Balearic Front, using the velocity field obtained from a numerical simulation of the surface circulation. As in the previous work, the problem is approached from the point of view of dynamical systems theory. We focussed on transport associated with the interaction of the front with one, or two eddies. The numerical simulation provides us with an Eulerian view of the flow and we use the dynamical systems approach to identify relevant hyperbolic trajectories and their stable and unstable manifolds which are used to uncover a Lagrangian structure of the front-eddy system. The interplay of the Eulerian and Lagrangian points of view is significant. The Eulerian flow structures are suggestive of the features requiring the more quantitative Lagrangian transport analysis. We showed that Lagrangian transport in the system is effected by the turnstile mechanism whose temporal evolution reveals the spatio-temporal routes along which transport occurs. We also showed that different transport routes are possible depending on whether the front interacts with one or two eddies. Moreover, we considered the transport implications associated with the transition between the one and two eddy situation and showed how some transport routes can be activated or deactivated due to the transition. We expect that this type of transition between different Eulerian flow structures is common in geophysical flows and that it will involve a variety of different Lagrangian scenarios beyond those studied in this paper. We introduce a kinematic model that will enable further studies of transport involving a variety of different flow structures in different settings. In particular, studies of the kinematic model should provide insights into the nature of the change in hyperbolic trajectories and their stable and unstable manifolds associated with the "birth and death" of eddies. Further mathematical development from such insights will be crucial for understanding the implications for Lagrangian transport

in much more complicated front-eddy systems than those identified in our particular data set.

Acknowledgements

A.M.M. acknowledges the financial support from CSIC grants PI-200650I224 and OCEANTECH (No. PIF06-059). M. B. and S. W. acknowledge financial support from ONR Grant No. N00014-01-1-0769. We also acknowledge Vicente Fernández for providing us with data from the DieCAST simulations.

References

[1] H. Aref, *The development of chaotic advection*, Phys. Fluids **14(4)** (2002), 1315–1325.

[2] J. H. Bartlett, *Limits of stability for an area-perserving polynomial mapping*, Cel. Mech. **28** (1982), 295–317.

[3] C. Basdevant and T. Philipovitch, *On the validity of the "Weiss criterion" in two-dimensional turbulence*, Physica D **73** (1994), 17–30.

[4] A. S. Bower, *A simple kinematic mechanism for mixing fluid parcels across a meandering jet*, J. Phys. Oceanogr. **21** (1991), 173–180.

[5] M. Cencini, G. Lacorata, A. Vulpiani, and E. Zambianchi, *Mixing in a meandering jet: A Markovian approximation*, J. Phys. Oceanogr. **29(10)** (1999), 2578–2594.

[6] S. R. Channon and J. L. Lebowitz, *Numerical experiments in stochasticity and homoclinic oscillations*, Ann. New York Acad. Sci. **357** (1980), 108–118.

[7] D. B. Chelton, M. G. Schlax, R. M. Samelson, and R. A. de Szoeke, *Global observations of large oceanic eddies*, Geophysical Research Letters **34** (2007), L15606.

[8] W. A. Coppel, *Dichotomies in stability theory*, Lecture Notes in Mathematics, vol. 629, Springer-Verlag, New York, Heidelberg, Berlin, 1978.

[9] C. Coulliette and S. Wiggins, *Intergyre transport in a wind-driven, quasi-geostrophic double gyre: An application of lobe dynamics*, Nonlinear Processes in Geophysics **8** (2001), 69–94.

[10] R. Cucitore, M. Quadrio, and A. Baron, *On the effectiveness and limitations of local criteria for the identification of a vortex*, Eur. J. Mech. B/Fluids **18**, no. 2.

[11] D. Dietrich, *Application of a modified "a" grid ocean model having reduced numerical dispersion to the Gulf of Mexico circulation*, Dyn. Atmos. Oceans **27** (1997), 201–217.

[12] D. Dietrich, R. Haney, V. Fernández, S. Josey, and J. Tintoré, *Air-sea fluxes based on observed annual cycle surface climatology and ocean model internal dynamics: a non-damping zero-phase-lag approach applied to the Mediterranean sea*, J. Mar. Sys. **52** (2004), 145–165.

[13] J. Q. Duan and S. Wiggins, *Fluid exchange across a meandering jet with quasi-periodic time variability*, J. Phys. Oceanogr. **26** (1996), 1176–1188.

[14] S. Dutkiewicz, A. Griffa, and D. B. Olson, *Particle diffusion in a meandering jet*, J. Geophys. Res. **98(C9)** (1993), 16487–16500.

[15] V. Fernández, D. Dietrich, R. Haney, and J. Tintoré, *Mesoscale, seasonal and interannual variability in the Mediterranean sea using a numerical ocean model*, Progress in Oceanography **66** (2005), 321–340.

[16] G. Haller, *Finding finite-time invariant manifolds in two-dimensional velocity fields*, Chaos **10(1)** (2000), 99–108.

[17] ———, *Lagrangian structures and the rate of strain in a partition of two-dimensional turbulence*, Physics of Fluids **13** (2001), no. 11, 3365–3385.

[18] ———, *Lagrangian coherent structures from approximate velocity data*, Physics of Fluids **14** (2002), no. 6, 1851–1861.

[19] ———, *An objective definition of a vortex*, J. Fluid Mech. **525** (2005), 1–26.

[20] G. Haller and A. Poje, *Finite time transport in aperiodic flows*, Physica D **119** (1998), 352–380.

[21] D. Henry, geometric theory of semilinear parabolic equations, lecture notes in mathematics, vol. 840., Springer-Verlag: New York, Heidelberg, Berlin, 1981.

[22] K. Ide, D. Small, and S. Wiggins, *Distinguished hyperbolic trajectories in time dependent fluid flows: analytical and computational approach for velocity fields defined as data sets*, Nonlinear Processes in Geophysics **9** (2002), 237–263.

[23] N. Ju, D. Small, and S. Wiggins, *Existence and computation of hyperbolic trajectories of aperiodically time-dependent vector fields and their approximations*, Int. J. Bif. Chaos **13** (2003), 1449–1457.

[24] S. Louazel and B. L. Hua, *Vortex erosion in a shallow-water model*, Physics of Fluids **16** (2004), no. 8, 3079–3085.

[25] M. S. Lozier, L. J. Pratt, A. M. Rogerson, and P. D. Miller, *Exchange geometry revealed by float trajectories in the Gulf Stream*, J. Phys. Oceanogr. **27** (1997), 2327–2341.

[26] R. S. MacKay, J. D. Meiss, and I. C. Percival, *Transport in Hamiltonian systems*, Physica D **13** (1984), no. 1-2, 55–81.

[27] N. Malhotra and S. Wiggins, *Geometric structures, lobe dynamics, and Lagrangian transport in flows with aperiodic time-dependence, with applications to Rossby wave flow*, J. Nonlinear Science **8** (1998), 401–456.

[28] A. M. Mancho, E. Hernández-García, D. Small, and S. Wiggins, *Lagrangian transport through an ocean front in the North-Western Mediterranean Sea*, J. Phys. Oceanogr. **??** (2008), ??

[29] A. M. Mancho, D. Small, and S. Wiggins, *Computation of hyperbolic and their stable and unstable manifolds for oceanographic flows represented as data sets*, Nonlinear Processes in Geophysics **11** (2004), 17–33.

[30] ———, *A tutorial on dynamical systems concepts applied to Lagrangian transport in oceanic flows defined as finite time data sets: Theoretical and computational issues*, Physics Reports **437** (2006), 55–124.

[31] A. M. Mancho, D. Small, S. Wiggins, and K. Ide, *Computation of stable and unstable manifolds of hyperbolic trajectories in two-dimensional, aperiodically time-dependent vector fields*, Physica D **182** (2003), 188–222.

[32] S. D. Meyers, *Cross-frontal mixing in a meandering jet*, J. Phys. Oceanogr. **24** (1994), 1641–1646.

[33] P. D. Miller, C. K. R. T. Jones, A. M. Rogerson, and L. J. Pratt, *Quantifying transport in numerically generated velocity fields*, Physica D **110** (1997), 105–122.

[34] J. S. Muldowney, *Dichotomies and asymptotic behaviour for linear differential systems*, Trans. A.M.S. **283(2)** (1984), 465–484.

[35] K. Ngan and T. G. Shepherd, *Chaotic mixing and transport in Rossby wave critical layers*, J. Fluid. Mech. **334** (1997), 315–351.

[36] A. Okubo, *Horizontal dispersion of floatable particles in the vicinity of velocity singularities such as convergences*, Deep-Sea Research **17** (1970), 445–454.

[37] A. M. Rogerson, P. D. Miller, L. J. Pratt, and C. K. R. T. Jones, *Lagrangian motion and fluid exchange in a barotropic meandering jet*, J. Phys. Oceanogr. **29** (1999), 2635–2655.

[38] V. Rom-Kedar, A. Leonard, and S. Wiggins, *An analytical study of transport, mixing, and chaos in an unsteady vortical flow*, J. Fluid Mech. **214** (1990), 347–394.

[39] V. Rom-Kedar and S. Wiggins, *Transport in two-dimensional maps*, Arch. Rat. Mech. Anal. **109** (1990), 239–298.

[40] R. Samelson and S. Wiggins, *Lagrangian transport in geophysical jets and waves: The dynamical systems approach*, Springer-Verlag, New York, 2006.

[41] R. M. Samelson, *Fluid exchange across a meandering jet*, J. Phys. Oceanogr. **22** (1992), 431–440.

[42] Q. Schiermeier, *Churn, churn, churn*, Nature **447** (2007), 522–524.

[43] S. Wiggins, *Chaotic transport in dynamical systems*, Springer-Verlag, New York, 1992.

[44] ———, *The dynamical systems approach to Lagrangian transport in oceanic flows*, Annu. Rev. Fluid Mech. **37** (2005), 295–328.

[45] G.-C. Yuan, L. J. Pratt, and C. K. R. T. Jones, *Barrier destruction and Lagrangian predictabilty at depth in a meandering jet*, Dyn. Atmos. Oceans **35** (2001), 41–61.

[46] ———, *Cross-jet Lagrangian transport and mixing in a $2\frac{1}{2}$ layer model*, J. Phys. Oceanogr. **34** (2004), no. 9, 1991–2005.